Deposition of dry particles on a fin-and-tube heat exchanger by a coupled soft-sphere DEM and CFD

Turo Välikangas[a,*], Jakob Hærvig[b], Heino Kuuluvainen[a], Miikka Dal Maso[a], Petteri Peltonen[c], Ville Vuorinen[c]

[a] *Aerosol Physics Laboratory, Physics Unit, Tampere University, Finland*
[b] *Department of Energy Technology, Aalborg University, Denmark*
[c] *Department of Mechanical Engineering, Aalto University, Finland*

Abstract

In this study, a novel computational model is utilized for investigating fouling of two commonly encountered heat exchanger fin shapes in an air-conditioning application. The computational method utilizes the discrete element method (DEM) coupled with a large-eddy simulation (LES) framework. The fin-and-tube heat exchangers (FTHE) are investigated for three different Reynolds numbers (Re_{D_h} =243, 528, 793), three different particle sizes (D_p = 5, 10, 20 µm) and two different adhesive particle types based on the experimental values in the literature. The code is first benchmarked from the CFD and DEM viewpoints. A comprehensive fouling study of the FTHE's, consisting of altogether 36 simulations, is then carried out. The major numerical findings of the paper consist of the following four features. First, with low adhesive particles, the plain fin shape has a 3.45 higher volume fouling rate with Re_{D_h} =793 than at Re_{D_h} =264. With the herringbone fin shape, and the low adhesive particles, the volume fouling rate is 1.76 higher with Re_{D_h} =793 than at Re_{D_h} =264. Second, for the high adhesive particles, the plain fin has a 5.4 times higher volume fouling rate at Re_{D_h} =793 than for Re_{D_h} =264. The herringbone fin shape has a 3.92 times higher volume fouling rate with the highest Reynolds number of Re_{D_h} =793 compared to Re_{D_h} =264. Third, high adhesive particles have 3.0 times higher volume fouling rate than low adhesive particles for both fin shapes, all particle sizes and all Reynolds numbers combined. And finally, herringbone fins have 1.74 times higher volume fouling rate than plain fins for low adhesive particles. For high adhesive particles, herringbone has 1.8 times

higher volume fouling rate and when both particle types are summed together, herringbone has a 1.78 times higher volume fouling rate than the plain fin shape. As a major finding of the study, the high adhesive particle collection efficiency increases monotonously with the Stokes and Reynolds numbers while low adhesive particle collection efficiency poses a non-monotonous trend.
Keywords: fin-and-tube heat exchanger, herringbone fin, plain fin, CFD-DEM, soft sphere, dry-particle, fouling, large-eddy simulation

---

*I am corresponding author

Email addresses: turo.valikangas@tuni.fi (Turo Välikangas), jah@et.aau.dk (Jakob Hærvig), heino.kuuluvainen@tuni.fi (Heino Kuuluvainen), miikka.dalmaso@tuni.fi (Miikka Dal Maso), petteri.peltonen@aalto.fi (Petteri Peltonen), ville.vuorinen@aalto.fi (Ville Vuorinen)

1. Introduction

Globally around $10 - 20\%$ of the energy consumption in developed countries is used by the Heating Ventilation and Air Conditioning (HVAC) systems of buildings [1]. Almost half of the total energy consumption in buildings is due to air conditioning [1]. Commonly used type of a heat exchanger in the air conditioning unit is a Fin-and-Tube Heat Exchanger (FTHE). Inside the FTHE, heat is exchanged between the flowing air between the fins and the fluid flow in the tubes. The efficiency of a heat exchanger is defined as the ratio between the exchanged heat and the induced pressure drop [2]. Considering the complete heat transfer process, around $60 - 80\%$ of the resistance has shown to be on the air side [3, 4]. The most traditional design of a FTHE with plain fins [5, 6] can be made smaller by making the fin wavy [7, 8, 9]. In this way, smaller heat exchangers could be designed. Later, as enabled by louvered [10] and slit [11] fins even more compact heat exchangers have been made for various different air conditioning applications. Quite recently, vortex generators [12, 13] including winglet type flow actuators [14] have been proposed for enhancing heat transfer. Most of the previous CFD studies are conducted with ideal air without impurities. Therefore, new designs obtained with CFD are only valid for a new heat exchanger for a short period of time.

After long term operation, air impurities begin to accumulate inside the heat exchanger [15, 16, 17], commonly denoted fouling. Such fouling processes can be classified into wet and dry particulate fouling. The present work focuses on the dry particulate fouling. Dry particulate fouling process can be further divided into the nucleate and bulk fouling regimes [18]. Every fouling process will initially start with the nucleation regime where particles accumulate on the surface and form a deposition distribution. Later on, once the surfaces have been initially deposited by particles, the nucleation regime transitions typically towards the bulk fouling regime. At this stage the induced pressure drop from fouling is at its maximum in a specific operation point.

In HVAC applications, typical substances that contribute to fouling are dust and fibres that can originate from clothes, furniture and fur of domestic animals [19]. Fouling in dry

FTHE environments occurs mainly in the flow stagnation and recirculation regions [20]. Li et al. [21] propose that both particle size, shape and properties are important factors in the fouling process. While fouling of larger particles is dominated by inertial impact, smaller particles deposit by eddy transport and thermophoresis [22]. Due to the rather low temperature gradients in HVAC systems, thermophoresis is often negligible as one of the fouling mechanisms [23].

The challenges of studying FTHE by analytical and empirical means was pointed out by Siegel and Nazaroff [24]. They present a deterministic model for FTHE fouling with particle impaction, gravitational settling and Brownian diffusion. The authors pointed out deficiencies in the model for particles in the range of 5-20 micrometer scale particles having rather large initial velocity [24]. Another computational model by Inamdar et al. [25] was compared against the experimental results. The model was shown to predict the fouling trends in various different heat exchangers to an acceptable precision along with a qualitative estimation of the deposition distribution.

Experimental application field studies have been conducted to study the effect of the real fouling environment and the effect of fouling on the thermal hydraulic efficiency of the FTHE. Ahn et al. [19] showed that, in residential buildings, the mean fouling particle diameters typically range between 1-20 micrometers. In their study, they concluded that after 7 years, in both dry and wet cycle heat exchanger, the fouling can cause the pressure drop over the heat exchanger to increase up to 44% while the cooling capacity decreases $10-15\%$ [19]. Another study by Park et al. [26] shows that dry particle fouling causes $4-12\%$ decrease in heat transfer coefficient whereas, the pressure drop increases by $22-37\%$.

Above, FTHE's in HVAC context was discussed. Another branch of FTHE fouling investigations is related to heat recovery boilers. In such applications, the heat exchangers are exposed to ash and particulates originating from combustion processes. [27, 28, 29, 30]. The properties of the fouling particles in combustion fumes obviously differ drastically from the normal indoor fouling particle properties. The effect of fouling have been experimentally studied in the laboratory environment with various different standard dust types by various authors. An experimental study by Zhang et al. [31] for air conditioning application, con-

cluded that interrupted louvre fin shapes are more prone to fouling in a microchannel design than a planar fin. One of their main conclusions was that the interior of the heat exchanger with louvre fin is more vulnerable to fouling, whereas with the plain fin, the fouling occurs in the front surfaces. They emphasized that the type of the fin plays a prominent role in the fouling characteristics of the heat exchanger. [31] The microchannel heat exchanger and dry coolers were studied by Bell et al. [32, 33], who concluded an increase of up to 50% due to fouling on the pressure drop on the air side. Zhan et al. [34] studied the wavy fin-and-tube heat exchanger and concluded that areas that are most prone to fouling are the leading edge of the fins and the front part of the tubes. A very recent experimental study by Zhan et al. [18] investigated the fouling mechanism of wet-particle deposition and concluded that louvered fins are the most conducive to wet-particle deposition. They also pointed out that dry-particle and wet-particle fouling share several similarities. Yet, the fouling rate in dehumidifying conditions can be a factor of 5 to 7 times higher than the dry particle environment.

The numerical fouling studies conducted on an air conditioning application are very few. Zhan et al. [35] studied the bulk regime fouling with 50 µm particles with Reynolds-Averaged Navier-Stokes flow simulation and developed a model for the fouling thickness. The effect of particles sizes on the deposition areas on a metal foam heat exchanger has been studied by Sauret and Hooman [36] in laminar conditions. Kuruneru et al. [37] has developed and validated a CFD-DEM model to study fouling of a metal foam heat exhchanger. Kuruneru et al. [38] studied the fouling bulk regime of 25 µm particles in an oscillating unsteady laminar flow and made a comparison study between sawdust and sandstone type particles [39] in the metal foam heat exchanger. Kuruneru et al. [40] also studied fouling with 50 µm and with very low inlet velocity of around $0.1 m/s$, which is very rarely encountered in HVAC application. All these studies focus on the bulk regime fouling for a very simple tube bank geometry with surrounding metal foam porous area.

Based on the literature survey, fouling of the heat transfer surfaces is an important concern in heat exchanger design. There is a clear research gap for better understanding FTHE fouling processes by simulations which, not only model the fluid flow by CFD, but

also model the particle phase and the particle-surface interactions. The main objectives of the present study are listed as follows. First, a CFD-DEM model is benchmarked to model fouling processes in heat exchangers. Second, two different fin shapes with three different particle sizes, 3 typical inlet velocities and two different particle adhesive types are simulated to illustrate and to quantify, via a pioneering research approach, the fouling rate in the nucleation regime of the heat transfer surfaces. The first fin shape is a plain fin without fin forming. The other, very common fin shape used in the industry, is called the herringbone. The overall motivation is to find quantitative results, which can be used to asses the amount of fouling between the different fin shapes. Thereby, in larger scope, the study demonstrates a next level approach to develop enhanced heat transfer surfaces with lower pressure drop and higher heat transfer rates.

2. Details on the numerical domain and setup

The geometry in the present study is widely used in HVAC industry and has been studied by others as well Chokeman and Wongwises [9], Pirompugd et al. [41]. Two fin types are studied to illustrate the geometry effects on the fouling characteristics.

2.1. Computational domain

The computational domain is limited to one channel between the fins. The simulation domain is shown in Fig. 1 for the herringbone fins. For the plain fins, the geometry is otherwise exactly the same.

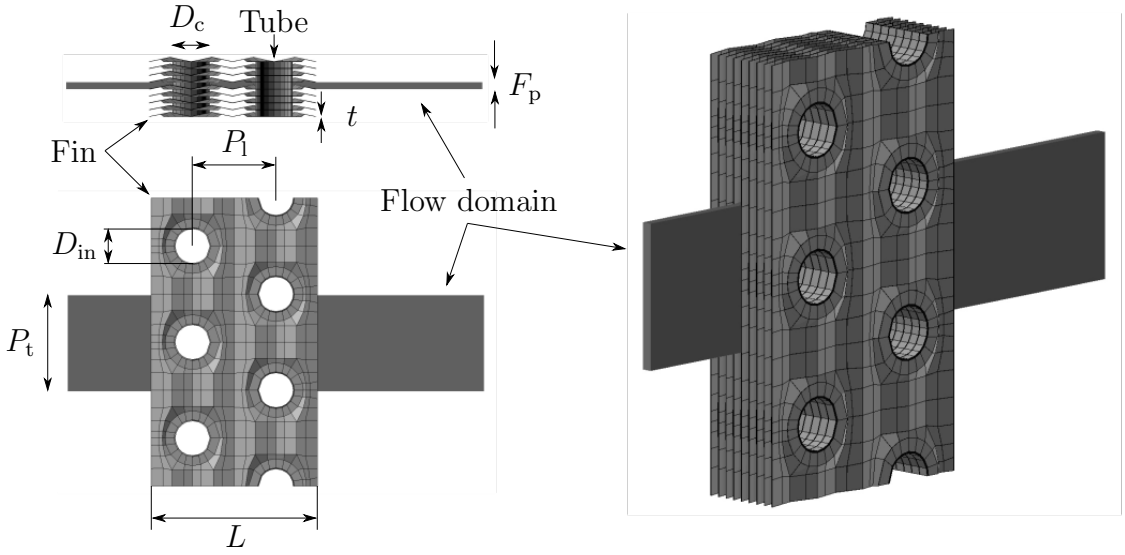

Figure 1: Illustration of the fin-and-tube heat exchanger geometry being simulated

The inlet is placed a distance of P_l upstream from the heat exchanger geometry to make sure the deposition process is independent of the inlet position. Similarly, the outlet is placed $2P_l$ downstream of the heat exchanger geometry. Further details on the geometries are provided in Table 1.

Table 1: Geometric dimensions for herringbone and plain fin shape.

Parameter	**Symbol/unit**	**Value**
Outside diameter of tube collar	D_c	9.76 mm
Longitudinal tube distance	P_l	22.0 mm
Transverse tube distance	P_t	25.4 mm
Number of tube row	n	2
Fin length along flow direction	L	44.0 mm
Fin pitch	F_p	1.81 mm
Fin thickness	t	0.115 mm
Herringbone amplitude	P_d	1.19 mm
Herringbone half wave length	X_f	5.5 mm

Throughout this study, the hydraulic diameter is used as a characteristic length scale of the flow. The hydraulic diameter is defined as:

$$D_\mathrm{h} = \frac{4 \cdot \text{free flow volume}}{\text{wetted area}} = \frac{4 \cdot \text{free flow area} \cdot \text{depth of the FTHE}}{\text{fin surface area} + \text{tube surface area}} = \frac{4(F_\mathrm{h})(P_\mathrm{t} - D_\mathrm{c})(2P_\mathrm{l})}{(4P_\mathrm{l}P_\mathrm{t} - 4\pi(\frac{D_\mathrm{c}}{2})^2) + ((F_\mathrm{h})2\pi D_\mathrm{c})} = 2.28\,\mathrm{mm} \tag{1}$$

where the flow is in a channel with the length $L = 2P_\mathrm{l} = 44$ mm, height $F_\mathrm{h} = F_\mathrm{p} - t = 1.695\,\mathrm{mm}$ and width $P_t = 25.4$ mm. In the normal direction of the fin, a staggered tube array is penetrated through the fin pack with the diameter of $D_\mathrm{c} = 9.76\,\mathrm{mm}$, longitudinal tube pitch $P_\mathrm{l} = 22\,\mathrm{mm}$ and transverse tube pitch $P_\mathrm{t} = 25.4\,\mathrm{mm}$. In this type of a flow, the flow length scale can be calculated as shown in equation [1]. The geometry details are shown in Table 1. The reference velocity used in this study is the average flow velocity at the minimum cross sectional area calculated as $U_\mathrm{max,avg} = U_\mathrm{inlet}\frac{A_\mathrm{inlet}}{A_\mathrm{min}}$, where $U_\mathrm{max,avg}$ is the maximum average flow velocity, U_inlet is the inlet flow velocity, A_inlet is the area of the inlet boundary and A_min is the area of the minimum cross section inside the heat exchanger.

In the present study, we use the no-slip boundary condition for velocity at the solid boundaries. Respectively, for pressure the zero gradient boundary condition is utilized at

the walls. At the inlet of the domain, constant velocity is prescribed while the zero gradient boundary condition is used at the outlet. At the lateral boundaries, periodic boundary conditions are used. The pressure is fixed at the outlet and assumed zero gradient at the inlet.

2.2. Governing equations for fluid flow

The governing equations for three-dimensional, incompressible, transient viscous flow with two-way coupling between the particle phase and the fluid through the heat exchanger are the continuity (2) and the momentum equations (3).

$$\frac{\partial(\alpha_{\mathrm{f}}\overline{u}_{\mathrm{i}})}{\partial x_{\mathrm{i}}} = 0 \tag{2}$$

$$\frac{\partial(\alpha_{\mathrm{f}}\overline{u}_{\mathrm{i}})}{\partial t} + \frac{\partial(\alpha_{\mathrm{f}}\overline{u}_{\mathrm{i}}\overline{u}_{\mathrm{j}})}{\partial x_{\mathrm{j}}} + = -\frac{\alpha_{\mathrm{f}}}{\rho_{\mathrm{f}}}\frac{\partial\overline{p}}{\partial x_{\mathrm{i}}} + \alpha_{\mathrm{f}}\frac{\partial}{\partial x_{\mathrm{j}}}((\nu+\nu_{\mathrm{sgs}})\frac{\partial\overline{u}_{\mathrm{i}}}{\partial x_{\mathrm{j}}}) - \frac{R_{\mathrm{pf}}}{\rho_{\mathrm{f}}} \tag{3}$$

where α_{f} is the local fluid volume fraction, $R_{\mathrm{pf}} = K_{\mathrm{pf}}(\mathbf{u} - \langle v\rangle)$ is the momentum exchanger with the particle phase. For the momentum exchange between the domains an implicit second-order accurate Crank-Nicolson scheme is used. The source of the momentum equation is the sum of the local particle-fluid forces ($F_{\mathrm{i,fluid}}$)

$$K_{\mathrm{pf}} = \frac{\alpha_{\mathrm{f}}|\sum_{\mathrm{i}}\mathbf{F}_{\mathrm{i,fluid}}|}{V|\mathbf{u} - \langle v\rangle|}. \tag{4}$$

In practice, the studied particle volume concentrations are in the order of $\phi = 5 \times 10^{-5}$, which corresponds to the 1-way coupling regime [42]. R_{pf} is small compared to the other terms and is neglected in the present study resulting in a 1-way coupling.

The governing equations are discretized by using a finite volume method and spatial terms are discretized by a second order accurate discretization scheme. The PISO (Pressure-Implicit with Splitting of Operators) [43] algorithm is used to couple the pressure and velocity fields. The CFD-DEM simulations are carried out with the open-source CFD-DEM solver called CFDEM (version 3.8.0) [44], which combines the CFD (version 5.0) toolbox OpenFOAM [45] with the DEM solver LIGGGHTS [46].

For accurate prediction of the trajectory calculation for the deposited particles, it is important to solve the flow field and the turbulence quantities correctly [20]. Because the particles are influenced by the largest, energy containing turbulent eddies throughout the flow, the larger eddies are resolved but the smaller ones are modelled. Such an approach is called Large Eddy Simulation (LES), where only the smallest scales of the turbulence structures are modelled while the larger scales are resolved directly. The sub-grid scale viscosity ν_{sgs} in this study is modelled by using a Wall-Adapting Local Eddy-viscosity (WALE) model with default parameters by Nicoud and Ducros [47], which is suited for wall-bounded flows as the eddy viscosity naturally goes to zero at the walls Mirzaei et al. [48].

As Nagaosa [49] concluded in the turbulence-model free study of a plain FTHE, the flow field inside the FTHE is fully laminar for $\text{Re}_{D_h} = 400$ (converted from Nagaosa [49] using the reference velocity and length scale as defined in the present study). A transition regime with both laminar and turbulent regions was reported for $\text{Re}_{D_h} = 400$-2000 and fully turbulent flow was observed for $\text{Re}_{D_h} = 2400$-3200. As a remark, in the present work $\text{Re}_{D_h} = 243$-793 which may involve both laminar and turbulent features. For the herringbone fin shape, the wavy fin shape induces a new lateral deviation to the flow field. Therefore, it will shift the spatial location of the transition as well as the critical Reynolds number for the transition.

2.3. Governing equations for particles

The collisions between the particles with each other and the fin surface is modelled with the soft-sphere discrete element method (DEM) approach [50]. If a particle i with the mass m_i and radius r_i, then the mass momentum of inertia can be calculated as $I_{\text{i}} = (2/5)m_{\text{i}}r_{\text{i}}^2$. The governing equation for the location $\boldsymbol{x}_{\text{i}}$ is given by 5 :

$$m_{\text{i}}\frac{\text{d}^2\boldsymbol{x}_{\text{i}}}{\text{d}t^2} = \boldsymbol{F}_{\text{i,con}} + \boldsymbol{F}_{\text{i,fluid}} \tag{5}$$

where the $\boldsymbol{F}_{\text{con}}$ is a contact force upon collision and $\boldsymbol{F}_{\text{fluid}}$ is the combined fluid force acting on the particle.

2.4. Fluid forces on particles

A Lagrangian approach is used to track the particles as they flow through the heat exchanger. In this study, particles with diameters of $d_\mathrm{p} = 5\,\mu\mathrm{m}$, $d_\mathrm{p} = 10\,\mu\mathrm{m}$ and $d_\mathrm{p} = 20\,\mu\mathrm{m}$ and with density of $\rho_\mathrm{p} = 2500\,\mathrm{kg\,m^{-3}}$ are being considered.

Here, we use the particle drag formulation by Benyahia et al. [51], which is based on the simulations by Hill et al. [52] and Koch and Hill [53], where the modified Stokes drag is defined as $C_d = (24/Re_p)F$, where $F = f(Re_p, \alpha_f)$. In the definition, Re_p corresponds to the particle Reynolds number while α_f corresponds to the particle volume fraction. By using this definition, a larger range of Reynolds numbers and particle volume fractions are covered.

2.4.1. Contact forces

The adhesive force between two spherical particles was originally studied by H.C. Hamaker in 1937 [54]. Hamaker concluded that the dominant forces of adhesion for two materials are the van der Waals and electrostatic forces. They originate from the continuous change of the electrical potential of atoms as the electrons circle around the core. The model that describes these forces is the Johnson-Kendall-Roberts (JKR) model that was originally developed by Johnson et al. [55]. The JKR model is suitable for the specific type of collision for which the Tabor parameter $\lambda_T = (4R\gamma^2/E^2D_{min}^3) > 3$ [56], where γ is the surface energy density, which is defined as half of the energy required to separate two particles in contact and D_min is the minimum separation distance, usually assumed to be 1.65 Å [57, 58].

Since the surface energy density is defined for a specific material to interact with itself, it is important to notice that the value cannot be used directly in the collision computations between two different materials. For this a new property called adhesion work $w = \sqrt{\gamma_1\gamma_2}$ [59] is used.

The contact forces in the normal direction of the surface that are modelled with the JKR model are the spring force $\boldsymbol{F}_\mathrm{spring,n}$, the adhesive force $\boldsymbol{F}_\mathrm{jkr,n}$ and the damping force $\boldsymbol{F}_\mathrm{damp,n}$:

$$\boldsymbol{F}_\mathrm{spring,n} = -\frac{4E}{3R}a^3\boldsymbol{n} \tag{6}$$

where n is the surface normal vector and a is the contact area.

$$\boldsymbol{F}_{\mathrm{jkr,n}} = 4\sqrt{\pi\gamma E a^3}\boldsymbol{n} \tag{7}$$

The effective Young's modulus is defined as $\frac{1}{E_{\mathrm{eff}}} = \frac{1-\nu_{\mathrm{i}}^2}{E_{\mathrm{i}}} + \frac{1-\nu_j^2}{E_j}$ and the effective radius $\frac{1}{R} = \frac{1}{r_{\mathrm{i}}} + \frac{1}{r_{\mathrm{j}}}$ for particle collision between two materials where E and ν are the Young's modulus and Poisson's ratio and the subscript corresponds to the colliding materials i and j. In order to model the dissipation of kinetic energy upon collision, a damping force $\boldsymbol{F}_{\mathrm{damp,n}}$ is used:

$$\boldsymbol{F}_{\mathrm{damp,n}} = -2\sqrt{\frac{5}{6}}\beta\sqrt{S_{\mathrm{n}}\boldsymbol{v}_{\mathrm{n}}} \tag{8}$$

where $\boldsymbol{v}_{\mathrm{n}}$ is the relative normal velocity, β is a parameter that takes into account the coefficient of restitution e as:

$$\beta = \frac{\ln(\mathrm{e})}{\sqrt{\ln^2(2) + \pi^2}} \tag{9}$$

S_{n} is parameter that takes into account the material properties as:

$$S_{\mathrm{n}} = 2E\sqrt{R\delta_{\mathrm{n}}} \tag{10}$$

where δ_{n} is the the overlap distance. In the tangential direction of the contact, the spring force $\boldsymbol{F}_{\mathrm{spring,t}}$ is used:

$$\mathbf{F}_{\mathrm{spring,t}} = -S_{\mathrm{t}}\Delta\mathrm{s}_{\mathrm{t}} \tag{11}$$

where $S_t = 8G\sqrt{R\delta_{s_t}}$ is a parameter for the particle properties and the δ_{s_t} is the tangential overlap. The effective shear modulus is calculated as $\frac{1}{G} = \frac{2-\nu_i}{G_i} + \frac{2-\nu_j}{G_j}$. As was done for the normal direction, a similar damping force $\boldsymbol{F}_{\mathrm{damp,t}}$ for the tangential direction is used:

$$\mathbf{F}_{\mathrm{damp,t}} = 2 - \sqrt{\frac{5}{6}}\beta\sqrt{S_{\mathrm{t}}m}\mathbf{v}_{\mathrm{t}} \tag{12}$$

where the $1/m = 1/m_i + 1/m_j$ is the effective mass and $\boldsymbol{v}_\mathrm{t}$ is the tangential velocity respect to the surface.

3. Computational model validation

Next, model validation results are discussed. First, a mesh sensitivity analysis on the pressure drop over both fin shapes is presented. Second, the collection efficiency of the FTHE for low adhesive particles at relevant particle sizes and two fin shapes is considered for different mesh resolutions. Additionally, the overall fluid dynamics and turbulence modelling is validated for a three-dimensional cylinder in crossflow. Third, the flow field inside the FTHE is validated against experimental results available in the literature. Fourth, the contact mechanics model is validated. Finally, the drag experienced by the particles is compared with the analytical Stokes equation and a particle number sensitivity study is carried out.

3.1. Mesh sensitivity assessment for fin-and-tube heat exchanger

In LES, it is of high priority to assess the mesh sensitivity of the results. From the viewpoint of particle transport, the energy containing flow scales should be resolved in order to capture the deposition process reliably [60, 61]. In the present study, we aim at resolving the flow field well, in order to capture the particle dispersion adequately. Thereby the sub-grid scale effect on particle dispersion is neglected. First, four different mesh resolutions are investigated by showing the pressure drop over the FTHE in Fig. 2 and the chosen mesh resolution is illustrated.

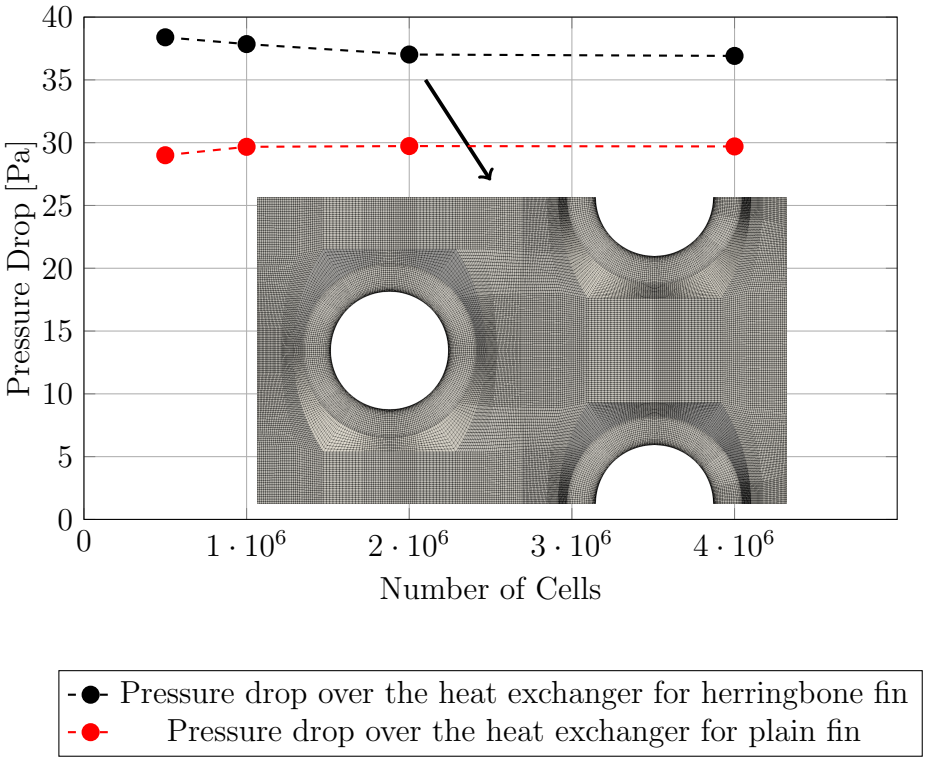

Figure 2: Pressure drop over the heat exchanger with respect to the cell count of the mesh with $Re_{D_h} = 793$ is shown as well as the chosen mesh resolution.

Next, the collection efficiency for low adhesive particles for the highest Reynolds number is shown for both fin shapes and three different particle sizes in Fig. 3. The same mesh resolution is used for the plain and herringbone fin shape, which was illustrated in Fig. 2. More information about the adhesiveness of the particle types is provided in Table. 2

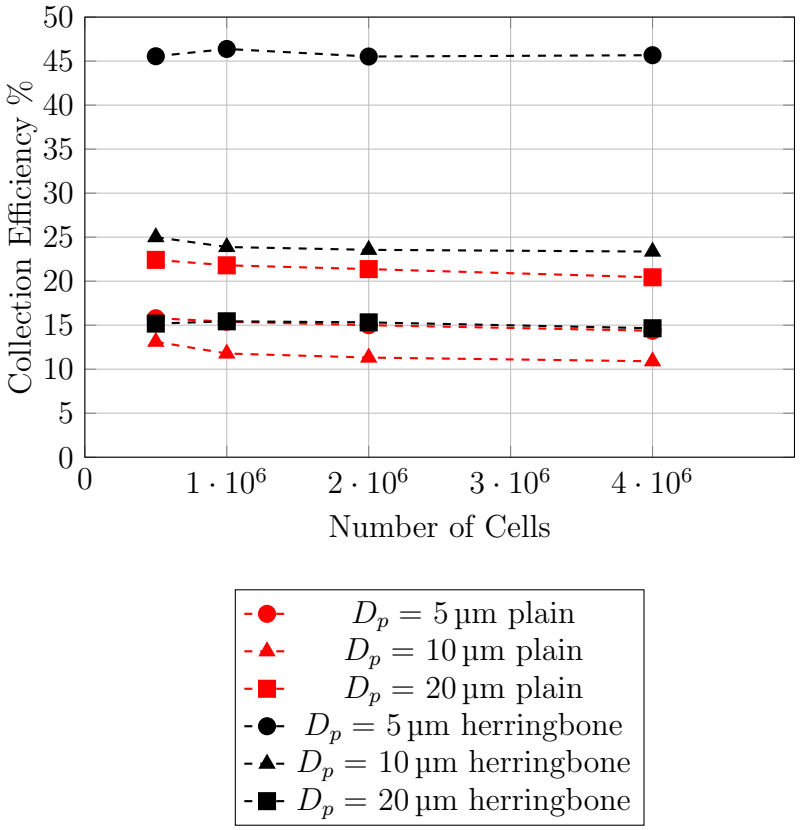

Figure 3: Mesh sensitivity study with respect to the cell count of the mesh with low-adhesive particles and $Re_{D_h} = 793$.

Based on the mesh sensitivity study, the results with the 2 million cell mesh in Fig. 3 deviate only 3% on average from the results with the 4 million cell mesh for the highest Reynolds number and low-adhesive particles. Such a scenario can be considered as the most conservative simulation case. Therefore, we conclude that the scales resolved by the 2 million cell mesh are sufficient to capture the particle transport in the present Reynolds number range. The low-adhesive particles are expected to bounce multiple times more from the surface in contrast to the high-adhesive ones and therefore the low-adhesive particles are influenced by the turbulent scales for a relatively long period of time. Thereby, we assume that the mesh resolution is sufficient for high-adhesive particles as well.

3.2. Single cylinder flow validation

In the previous section, the mesh with around 2 million cells was noted to provide acceptable accuracy. Next, using the same spatial resolution, the flow around a single cylinder is confirmed for the range of Reynolds numbers. The boundary layer flow around a cylinder is validated by comparing the drag coefficient and Strouhal number of a cylinder in a cross flow to the numerical results found from the literature for CFD studies [62, 63, 64] and experimental results [65]. The same y^+-value and maximum cell size was chosen as was selected to be sufficient in the mesh sensitivity study in section 3.1. The computational domain is 4D deep, 20D wide and 30D long.

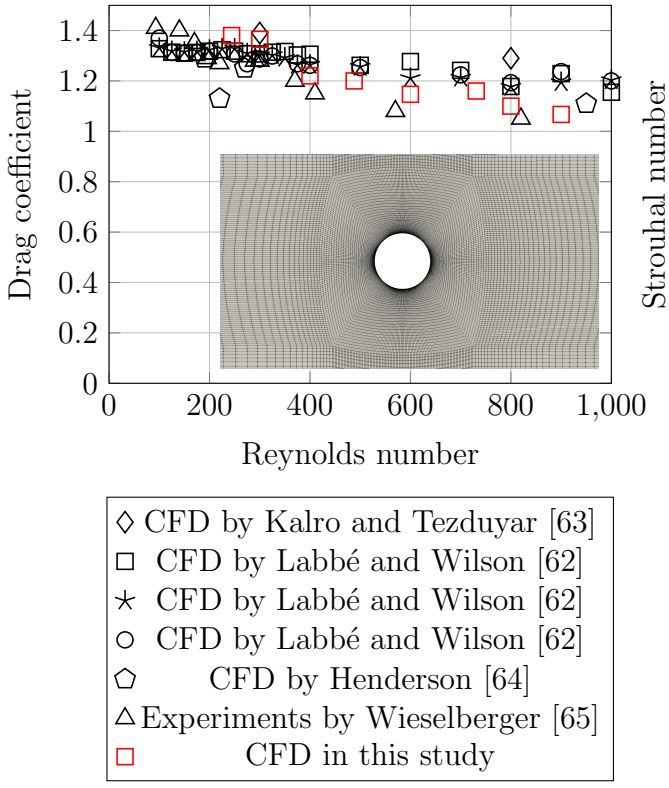

Figure 4: Comparison of the simulated three-dimensional drag coefficient and a boundary layer mesh illustration for flow around a cylinder without particles.

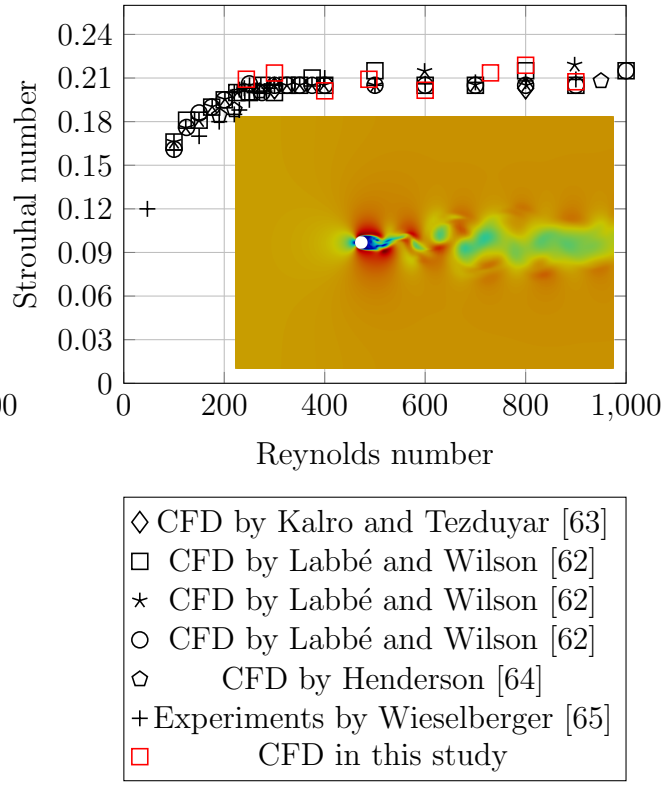

Figure 5: Comparison of the simulated three-dimensional Strouhal number and flow field illustration with $Re_D = 900$ for flow around a cylinder without particles.

3.3. Flow field validation inside a fin-and-tube heat exchanger

Model validation for the flow field inside the FTHE is carried out in Fig. 6 out by comparing the pressure drop over the heat exchanger to the experimental values by Chokeman and Wongwises [9] and Wang et al. [5]. The incident velocity range $U_{in} \in [1, 3]$ m/s corresponds to the $Re \in [243, 793]$.

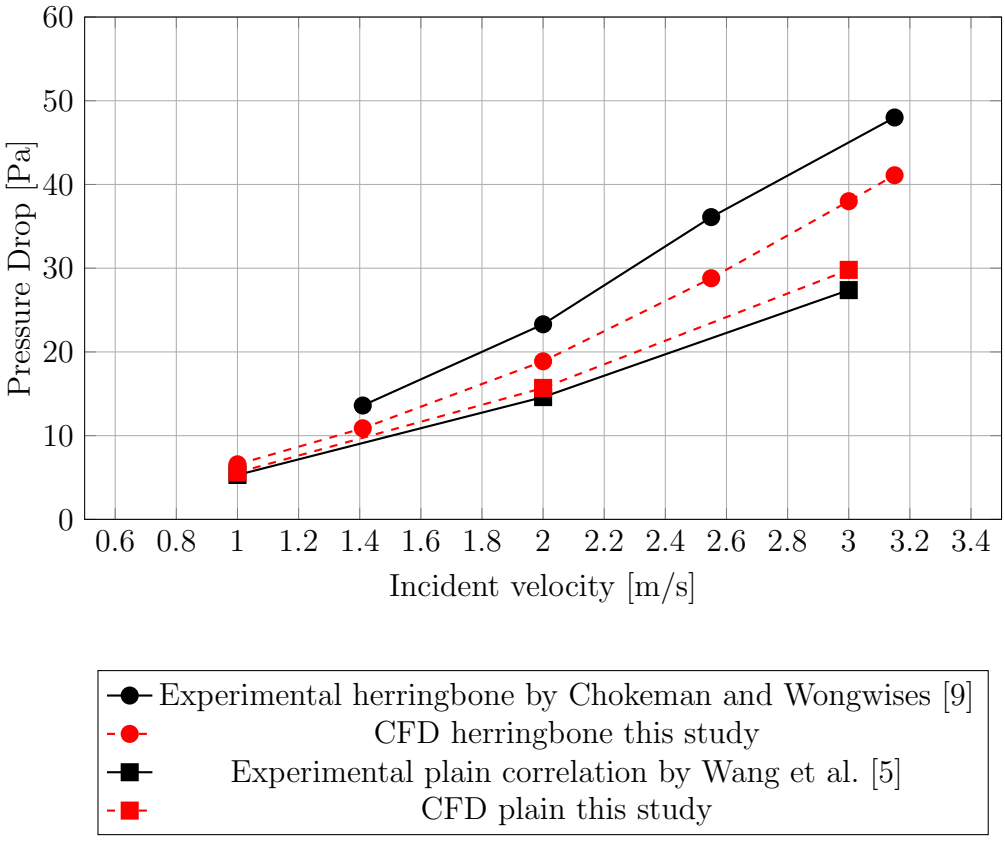

Figure 6: Simulated pressure drop over the heat exchanger compared to the experimental results found from the literature for both plain and herringbone fin shape.

The agreement with the experiments Wang et al. [5] and the simulated plain fin is good. Slightly more deviation can be seen for the herringbone fin shape [9]. The difference can be caused by the non-matching boundary conditions such as the turbulence level of the inlet flow. However, based on the numerical results presented in Fig. 6, we conclude the present model to be quantitatively reliable.

3.4. Particle number sensitivity study

A simple comparison was first performed between the analytical equations and the CFD-DEM framework to validate the drag force for individual particles. Settling velocity for all particle sizes and the stopping distance for all particle sizes with the corresponding initial velocities used in present study was compared to the analytical values derived from the Stokes drag law. A mean error of 1% was seen between the analytical and the value calculated with the CFD-DEM model used in present study.

To ensure that the collection efficiencies being reported are independent of the number of particles being simulated, simulations with 2500, 5000, 10,0000, and 20,000 particles was performed. The amount of particles is closely related to the computational resources required to perform the simulations. Therefore it is important to inject as few particles as possible to save in computational expenses.The collection efficiencies are $C_{20000} = 23.43\%$, $C_{10000} = 23.64\%$, $C_{5000} = 22.86\%$ and $C_{2500} = 23.08\%$ as shown in Fig. 7. For good visual illustration with reasonable computational cost, 10,000 particles were chosen for the number of simulated particles in all simulations.

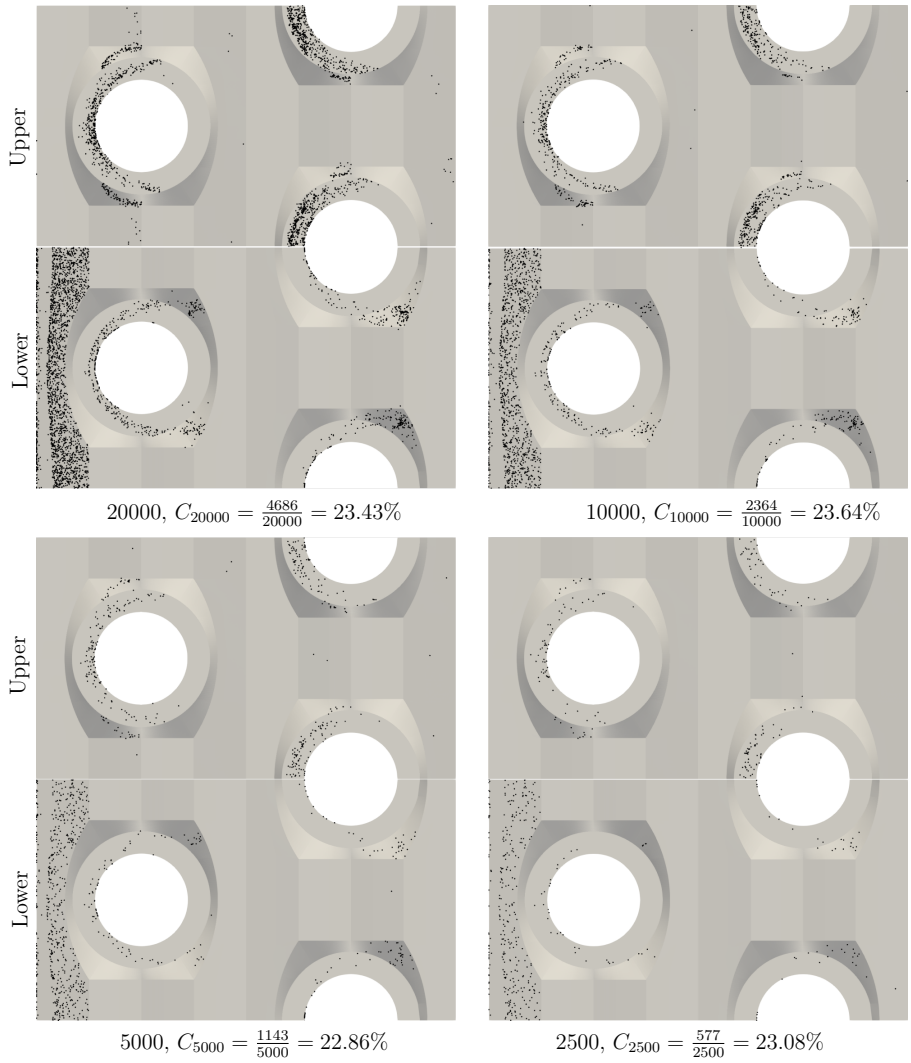

Figure 7: Illustration of the deposition distributions for both upper and lower fin for different amounts of $D_p = 10\,\mu\text{m}$ low adhesive particles and $Re_{D_h} = 732$, from left to right and upper to lower, 20000, 10000, 5000 and 2500 particles (size of the particles is multiplied by a factor of 30).

3.5. Contact mechanics validation

As a last demonstration of the model functionality, the contact mechanics between a particle and surface is validated by investigating the bouncing motion of a 6 mm Teflon particle impacting a soda glass surface. The material properties used for the comparison are tabulated in Table 3 in the Appendix.

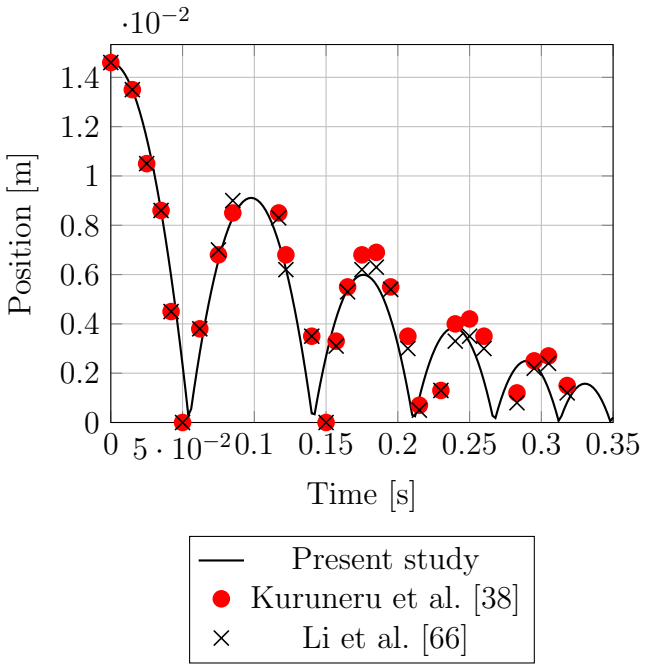

Figure 8: The position of a 6 mm Teflon ball respect to a soda glass surface.

The height of each individual bounce was seen to be almost identical with the reference values found from the literature [38, 66]. Thereby, we conclude that the contact mechanics for the particle impact with a wall surface is correctly implemented.

4. Particle property selection based on critical velocity measurements

In the context of particle-surface impact, the term 'critical velocity' refers to the incident velocity threshold under which a particle will stick to the surface. In practice, critical velocity depends on the particle properties (size, density, Young's modulus, Poisson's ratio, surface energy density and shape) as well as surface properties (Young's modulus, Poisson's ratio, surface energy density and surface roughness) [59]. Herein, a major effort is carried out to collect literature data on critical velocities in order to deduce and justify a meaningful parameter range for the simulations.

4.1. Description of the simulated properties

The particle concentration, size distribution and HVAC working conditions of the FTHE can be arbitrary. The fouling process is very slow and can be measured in months or years. A fouling process consists of a chain of events, where first, the smaller particles with higher critical velocity will start to deposit on the surface. For a clean surface, the critical velocity of larger particles is too low and therefore they will just rebound on the surface and re-entrain to the flow. This means that in the start of the nucleation regime, the smaller particles start to deposit on the surface and change the adhesion mechanics of the surface for the larger particles. This increases the critical velocity and therefore increases the amount of deposited larger particles. Because of the complexity of the fouling process and the variety in particle properties in the real application, it is essential to simplify the process of selecting the material properties so that the results are repeatable and comparable.

The material properties selection process is based on the critical velocity of a specific particle size. The information found in the literature on different particle and surface pairs and their critical velocity is shown in Fig. 9. Based on this figure, the critical velocities are typically in the range of $U_{\text{crit}} \in [0.1, 5]$ for $D_p \in [1, 20]$ µm. A relation between the particle diameter and the critical velocity can be observed from this data. Therefore, even with no information on the material of the particles or the deposition surface, we can assume that by using values that corresponds to the minimum and maximum of the data set, the results will represent both extremes of the particle types encountered in the real application. When the

contact mechanics of the chosen properties for a specific particle size are investigated further in Fig. 10, we can observe the restitution curve for each particle-surface pair, here for the $D_p = 20\,\mu\text{m}$. Finally, in Fig. 11, the impact kinetics of the collision with the aforementioned properties is illustrated for both adhesive levels with the same incident velocity. All the chosen pairs that lead to the size specific critical velocity are tabulated in the Appendix in Table 4.

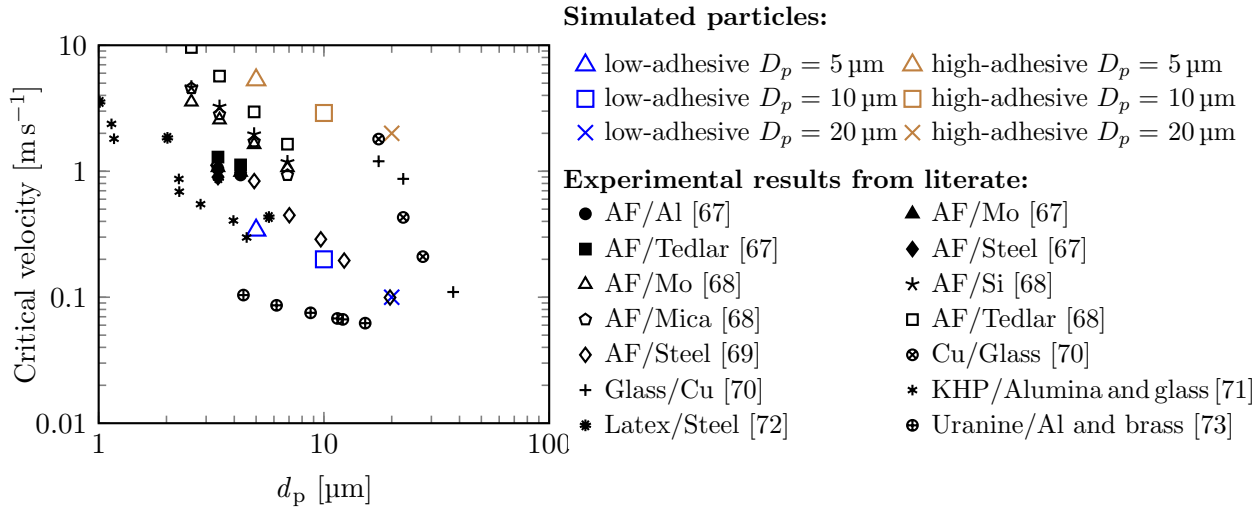

Figure 9: Comparison between experimental results from the literature and simulated particles in this study.

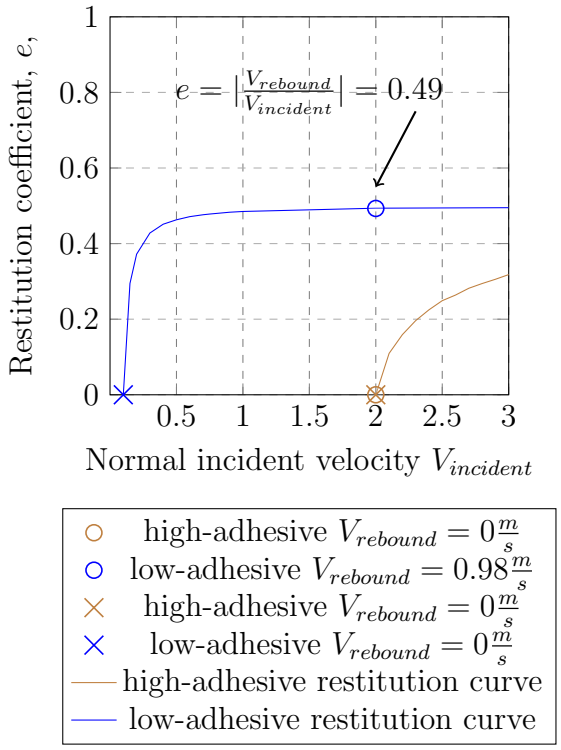

Figure 10: Restitution coefficient with respect to the incident velocity for the corresponding 20μm particles illustrated described in Fig. 9.

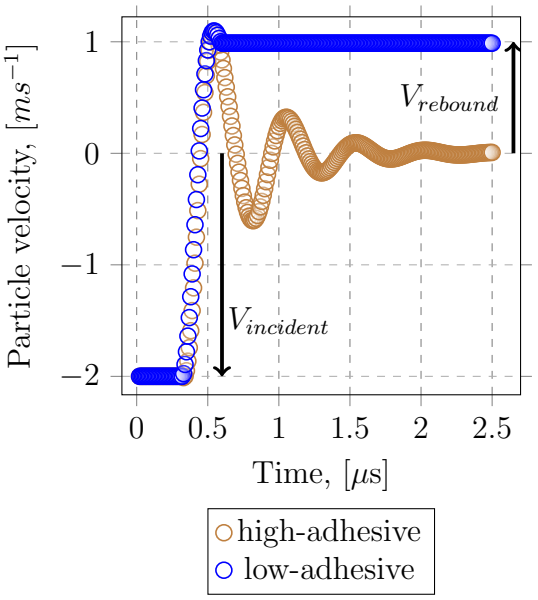

Figure 11: Velocity of particles during the impact for the corresponding particles described in Fig. 10, $D_p = 20\,\mu m$ with incident velocity of $V_{indicent} = 2$ m s^{-1}

4.2. Non-dimensional groups

A fouling process of a FTHE can be characterized by six parameters, namely the flow Reynolds number Re_{D_h}, the particle Stokes number $\mathrm{St}_{\tau_\mathrm{e}}$, the adhesion parameter Ad, the elasticity parameter λ, the density ratio χ and the particle to hydraulic diameter ratio ϵ further discussed in what follows.

The Reynolds number is defined as $\mathrm{Re}_{D_h} = U_{\max} D_\mathrm{h}/\nu$. Note that the used definition is based on the hydraulic diameter calculated in equation (1), the characteristic velocity at the minimum cross sectional area $U_{\max,\mathrm{avg}}$ and the dynamic viscosity $\nu = 15\,\mu\mathrm{m}^2/\,\mathrm{sec}$. The Stokes number $\mathrm{St}_{\tau_\mathrm{e}} = \tau_\mathrm{e}/\tau_\mathrm{f}$. The parameters that define the adhesiveness of the particles are the adhesion coefficient and elasticity parameter that are defined as $\mathrm{Ad} = \frac{\gamma}{U_{\max}^2\ \rho_\mathrm{p}\ d_\mathrm{p}}$ and $\lambda = \frac{E_\mathrm{eff}}{U_{\max}^2\ \rho_\mathrm{p}}$ [59]. Finally, the density ratio $\chi = \rho_\mathrm{f}/\rho_\mathrm{p} = 0.0005$ and the particle diameter $\epsilon = d_\mathrm{p}/D_\mathrm{h}$.

Although the fouling process is a slow process, the computational resources allow us to perform LES simulations of few-tenth of a second. For this reason, the volume fraction $\phi = \dot{V}_p/(\dot{V}_p + \dot{V}_f)$ of the particles at the inlet is increased to a higher value and kept constant between the different cases. The concentration value is kept low enough so that its effect on the flow field is negligible. The volume fraction being $\phi = 5 \cdot 10^{-5}$ for all the simulations. As these values are smaller than 10^{-4}, their effect on the flow field can be neglected [74]. The mass coupling parameter for the simulations is kept under 0.1 for all simulations to ensure that the mass coupling effects are unimportant [75]. The coefficient of restitution $e = 0.5$ is kept constant for all the particle types. An overview of the simulations carried out in this study is provided in Table 2.

Table 2: Details of the simulations performed in this study: ID is the identifier number of each case, non-dimensional particle diameter $\epsilon = d_\mathrm{p}/D_\mathrm{h}$, flow Reynolds number $\mathrm{Re}_{D_h} = U_\mathrm{max} D_\mathrm{h}/\nu$, Stokes number based on the eddy turnover time $\mathrm{St_e} = \rho_\mathrm{p} d_\mathrm{p}^2 U_\mathrm{max}/(18\mu_f D_\mathrm{h})$, the elasticity parameter $\lambda = E_{eff}/(\rho_\mathrm{p} U_\mathrm{max}^2)$, the adhesion parameter $\mathrm{Ad} = w/(\rho_\mathrm{p} U_\mathrm{max}^2 d_\mathrm{p})$ and name of the fin shape

Re_{D_h}=264		Re_{D_h}=528		Re_{D_h}=793		Fin shape
			ϵ=0.0021			
$\mathrm{St_e}$=0.16	λ=14.4×10^5	$\mathrm{St_e}$=0.31	λ=3.6×10^5	$\mathrm{St_e}$=0.47	λ=1.6×10^5	
ID	Ad	ID	Ad	ID	Ad	
1	0.82	2	0.2	3	0.09	Plain
4	27.7	5	6.9	6	3.1	Plain
7	0.82	8	0.2	9	0.09	Herringbone
10	27.7	11	6.9	12	3.1	Herringbone
			ϵ=0.0043			
$\mathrm{St_e}$=0.62	λ=14.4×10^5	$\mathrm{St_e}$=1.24	λ=3.6×10^5	$\mathrm{St_e}$=1.86	λ=1.6×10^5	
ID	Ad	ID	Ad	ID	Ad	
13	0.41	14	0.1	15	0.046	Plain
16	13.8	17	3.45	18	1.53	Plain
19	0.41	20	0.1	21	0.046	Herringbone
22	13.8	23	3.45	24	1.53	Herringbone
			ϵ=0.0087			
$\mathrm{St_e}$=2.49	λ=14.4×10^5	$\mathrm{St_e}$=4.97	λ=3.6×10^5	$\mathrm{St_e}$=7.47	λ=1.6×10^5	
ID	Ad	ID	Ad	ID	Ad	
25	0.2	26	0.05	27	0.022	Plain
28	6.91	29	1.73	30	0.77	Plain
31	0.2	32	0.05	33	0.022	Herringbone
34	6.91	35	1.73	36	0.77	Herringbone

5. Results and Discussion

Then the collection efficiency is shown with respect to the Reynolds number as well as Stokes number and adhesion parameter. Finally, an example is provided on the practical relevance and applicability of the present results.

5.1. Flow visualisation

Particles are inserted to the computational domain with the mean inflow velocity. An illustration of the flow field inside the heat exchanger and the upper and lower fins is provided in Fig. 12.

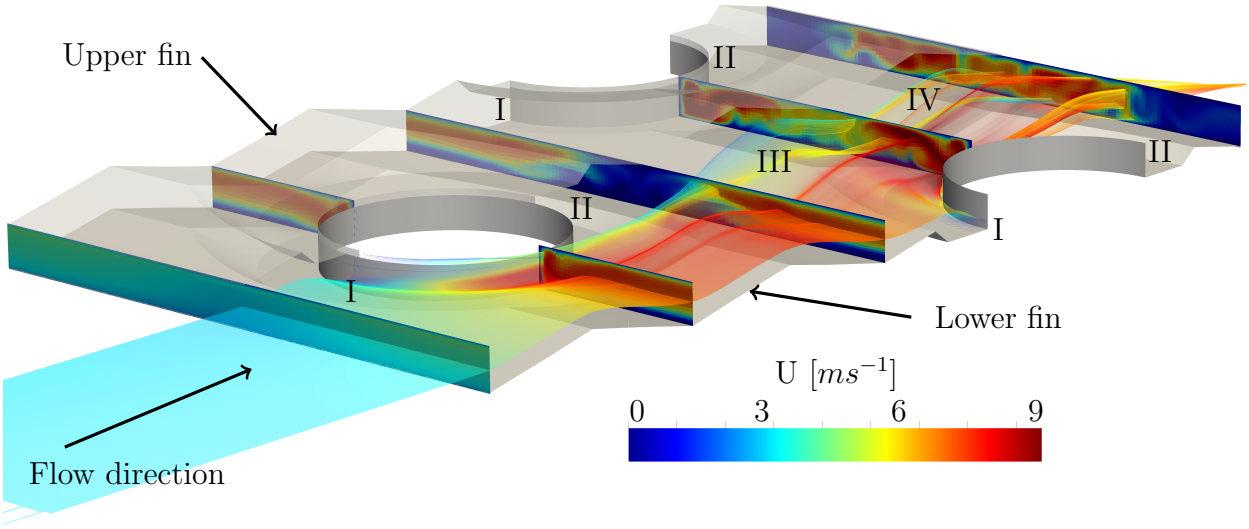

Figure 12: Illustration of the flow field and the upper and lower fin with respect to the flow direction with $Re = 793$.

It is noted how the laminar inflow impinges on the tube surface (I). Based on the literature, this point corresponds to a major region of particle deposition in various FTHE applications [34, 35]. Behind the tubes, a recirculation region (II) is formed. Such regions experience typically rather poor heat transfer characteristics [12]. Then, the flow undergoes transition from laminar to turbulent (III) while the flow is qualitatively relatively turbulent with incoherent features close to the outlet boundary (IV). We note that the channel height and cylinder diameter based Reynolds numbers are respectively 312 and 1800. Hence, the

flow is not fully turbulent from the viewpoint of standard channel flow but, instead, the unsteady cylinder wake provokes dynamic and incoherent flow features. Please see Nagaosa [49] for further information.

5.2. Fouling locations

The deposition locations for plain fins are shown from the upstream side in Figs 13- 14. The results with D_p =10 µm particles ($0.62 \leq St \leq 1.86$) are shown in Fig. 13. For St =0.62 the particle timescale is small from the flow timescale viewpoint and hence they will most likely follow the flow streamlines. For St =1.24, the particle timescale is of intermediate size and it is more likely for the particles to deviate from the streamline. For St =1.86, the directional change of the flow, due to e.g. tubes in the flow, enables large proportion of the particles to escape from the streamline and collide with the surface. After the particles have deviated from the streamline, the low-adhesive particles that hit the surface will bounce away from the surface and only stick during the next consecutive collisions. If the momentum of the particles is low enough, the particles will bounce multiple times on the tube surface and stick when the impact velocity is lower than the critical velocity. (I) If the momentum is high enough, the particles will bounce from the tube surface and reach the fin surface. Higher initial momentum will lead to larger amount of deposited particles on the fin and lower amount on the tube surface (II and III). In contrast, the high adhesive particles will most likely stick at the first collision, excluding the ones that have accelerated with the flow to achieve an impact velocity high enough to enable the particles to bounce, re-entrain to the flow and even hit the fin surface (IV). In fact, we have noted that the qualitatively, very similar trends on particle deposition would be noted for 5 µm ($0.16 \leq St \leq 0.47$) and 20 µm ($2.49 \leq St \leq 7.47$) particles. Fig. 13 shows deposition locations for plain fins, for particles with different characteristic features such as ID, Re, St, λ and Ad. The non-dimensional numbers and the ID of the simulation corresponds to the ones tabulated in Table. 2. Fouling locations for IDs 1-12 (D_p =5 µm) and 24-36 (D_p =20 µm) are provided in the Appendix.

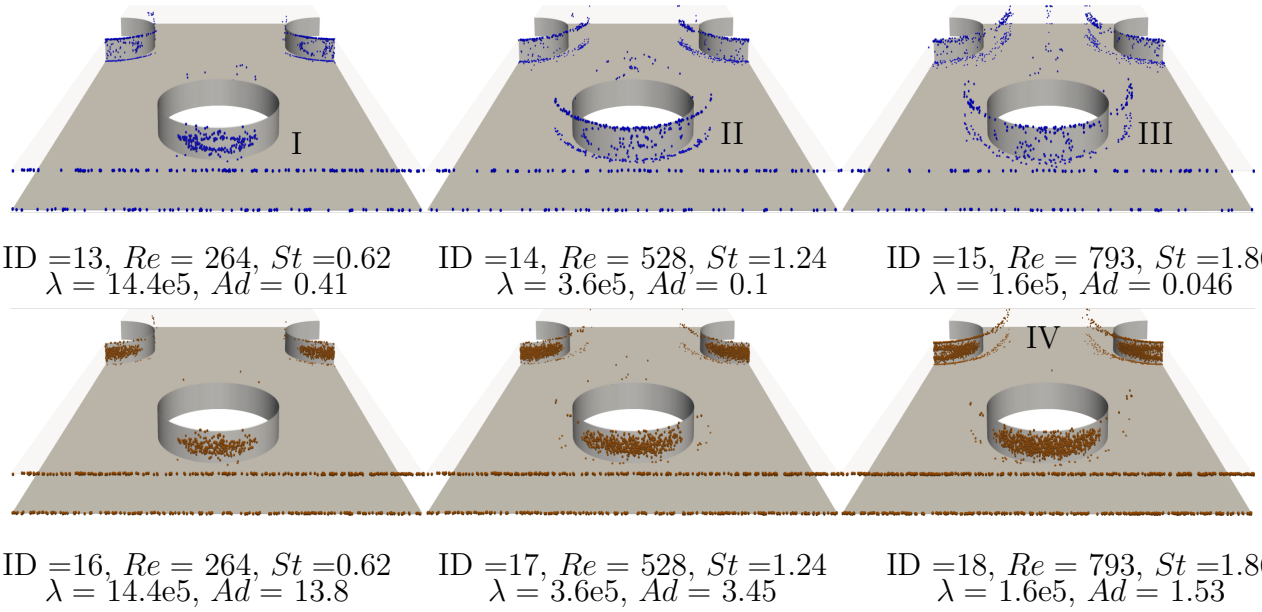

Figure 13: Deposition locations for plain fin with $D_p = 10\,\mu\text{m}$ • low-adhesive and • high-adhesive particles (size of particles increased by a factor of 30).

For all parameter values the qualitative trends are rather similar: most particles will deposit on the front side of the tubes. The deposition location results illustrate that with the ID =13, with the lowest Reynolds number and low adhesiveness, the particles at the center of the flow field will have just enough momentum so that they will bounce once and only deposit if they will hit the surface multiple times. Therefore only few particles will deposit in the middle of the tube. With the higher Reynolds number (ID=14 and ID=15) the particle inertia increases to a level that is enough for the particles to escape from the surface after the collision and therefore the tube surface will have less and less deposited particles. When the ID=15 is compared to ID=14, it can be seen that when the Reynolds number is even higher, the particles will start to deposit on the fin after the collision with the tube surface. With the higher adhesion levels (ID=16-18), the particles will deposit on the tube when they deviate from the streamlines and only rarely bounce back and deposit on the fin. For ID=18, an empty region can be seen on the second tube row where less particles have deposited on the middle of the tube. This is due to the fact that as the flow speed is increased in the middle of the channel between the fins, the particles will have

just high enough impact velocity so that they will bounce back, even though there exists a strong adhesive force between the particles and the fin. The low adhesive case with the highest Reynolds number, ID=21, is the only case where no particles are not deposited on the downwind side of the second tube row.

For the herringbone fins, the deposition locations are demonstrated for both upper and lower fins separately. The findings for the herringbone case are consistent with the plain fin cases above. Due to its wavy shape, the number of deposited particles is observed to be higher for the herringbone fin cases. As the particles enter the heat exchanger, the flow is initially guided towards the upper fin while most of the particles first hit the first wave of the lower fin (I). As for the ID=19 and ID=22, the deposition locations are almost identical between the cases. This means that in these cases, when the particle hits the surface, the impact velocity is under the corresponding critical velocity. Therefore, the adhesiveness of the particle does not affect the fouling process in these situations. The deposition surface at the trailing edge of the upper fin (II) shows how the fin shape is mixing the flow and causing the particles to hit the surface in a chaotic manner. For the low Reynolds number cases, particles are seen to deposit behind the tubes (III), in contrast to the higher Reynolds number cases where almost no particles are seen in the recirculation region. When the Reynolds number is increased, for low-adhesive particles, the flow accelerates particles impact velocities over the critical velocity and therefore, less particles deposit on the surface of the fin. The results for ID=19-24 are shown in Fig. 14.

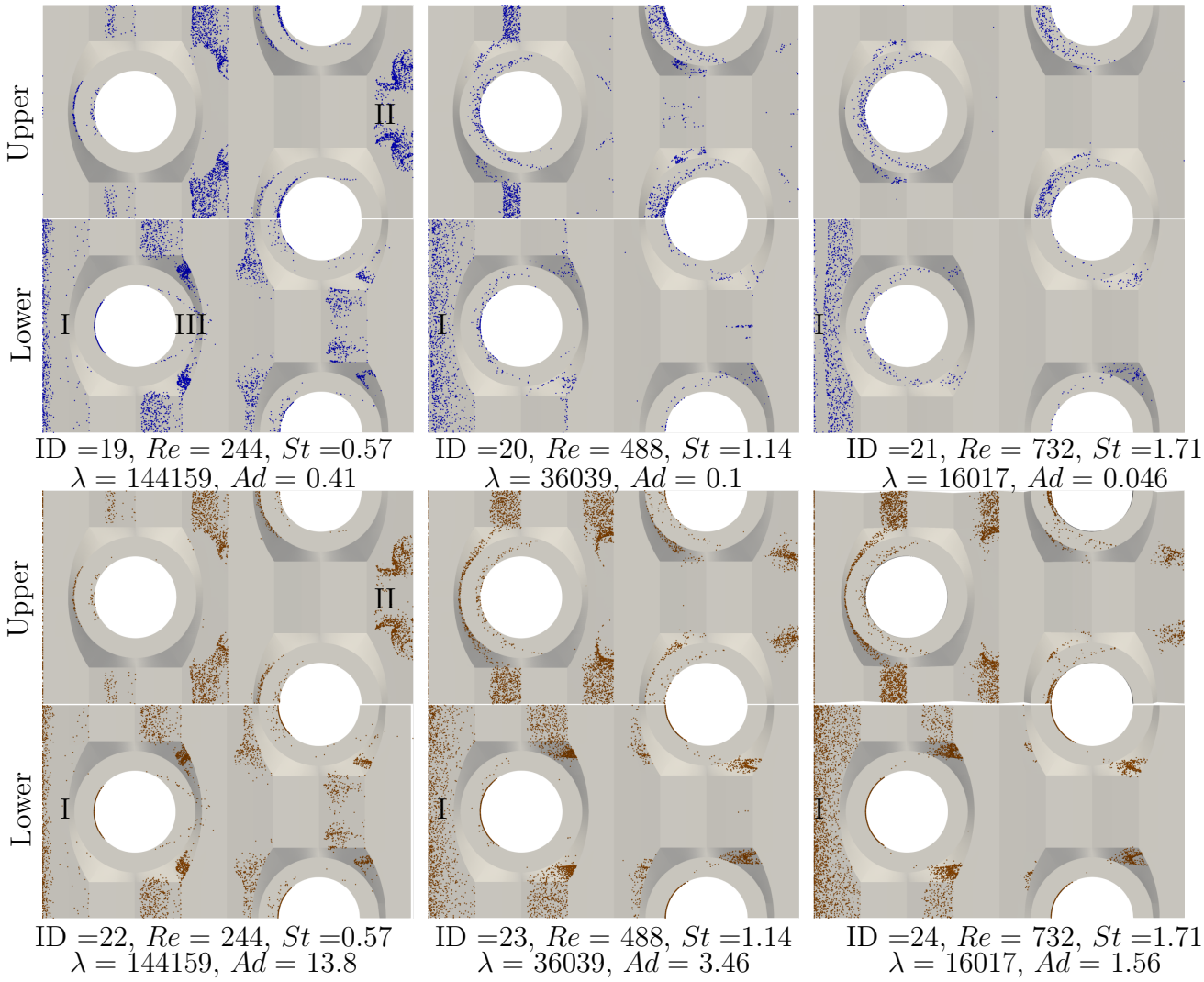

Figure 14: Deposition locations for lower and upper fin separately with D_p = 10 µm • low-adhesive and • high-adhesive particles.

5.3. Collection efficiencies

The fin collection efficiency can be defined as the ratio of the deposited and the inserted particles. It is clearly noted from Figs. 15-16 that, for high adhesive particles the collection efficiency will increase along with Reynolds number. The main reason for this phenomenon is the Stokes number, which increases along with the Reynolds number: the higher the Stokes number the more likely a particle deviates from the streamline. For low adhesive particles, the deposition process is much more complicated since the deposition rarely takes

place at the first collision. The process can be described with a series of collisions that eventually lead to the deposition of a particle. Based on the results on Figs. 15-16 there exists a non-monotonous trend between the Reynolds number and the collection efficiency. A maximum in the collection efficiency for the low-adhesive particles is observed between the ID=9 ($D_p = 5\,\mu m$ Re_{D_h} =793, St =0.47, Ad =0.09 and $\lambda = 1.6 \times 10^5$) and ID=19 ($D_p = 10\,\mu m$, Re_{D_h} =264, St =0.62, Ad =0.41 and $\lambda = 14.4 \times 10^5$). The results regarding the collection efficiency are reported in Figs. 15 -17 with respect to the Stokes number. It can be noted that a higher Stokes number does not necessarily lead to a higher collection efficiency or higher rate of fouling.

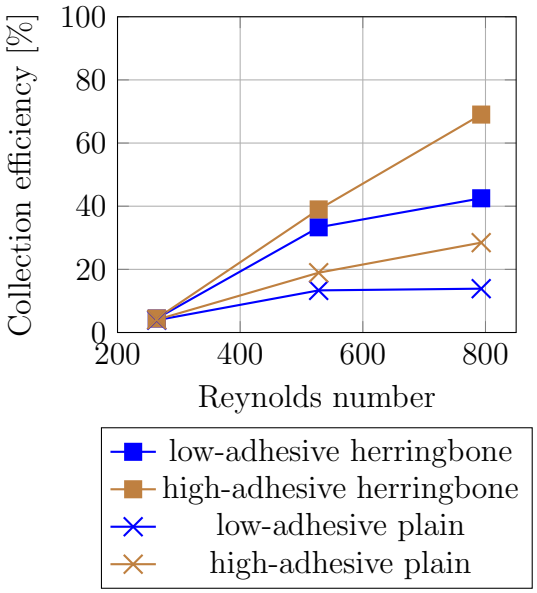

Figure 15: Collection efficiencies for $D_p = 5\,\mu m$

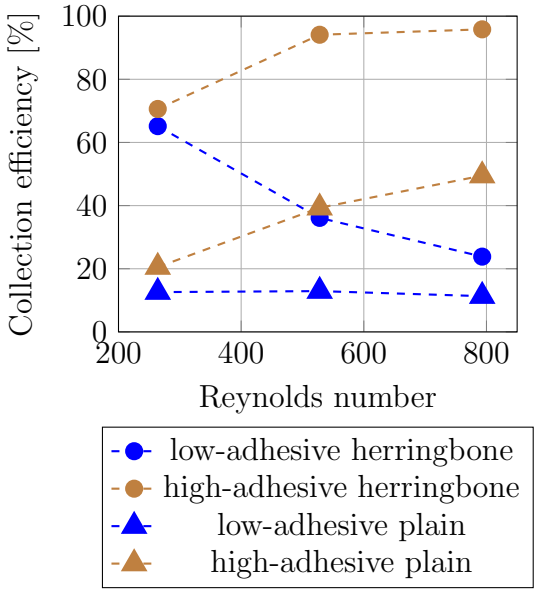

Figure 16: Collection efficiencies for $D_p = 10\,\mu m$.

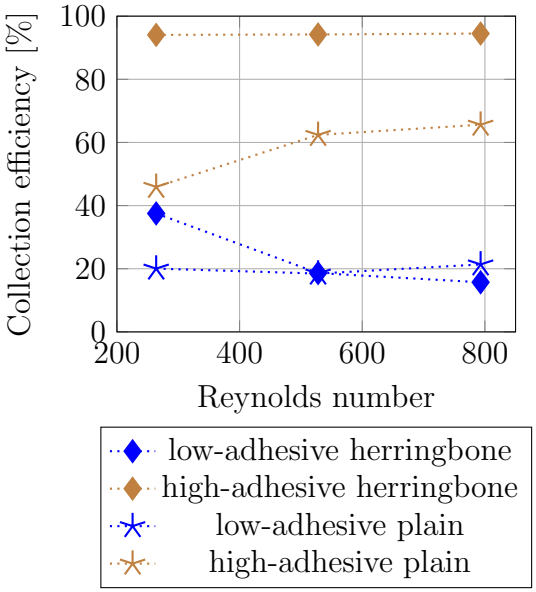

Figure 17: Collection efficiencies for $D_p = 20\,\mu m$.

In Fig. 18, the collection efficiency is shown with respect to the Stokes number. A conclusion can be made that a higher Stokes number does not always correlate to a higher collection efficiency and therefore a higher rate of fouling. For high adhesive particles the collection efficiency is shown to be a function of the Stokes number. But when investigated

more carefully, different particle size classes will lead to a small difference in the adhesive properties and therefore to a discontinuation in the collection efficiency. Thus, in fouling investigations, one should not only consider St and Re but also take into account the particle adhesiveness (Ad) and the elasticity parameter (λ) which further depend on the adhesion work, Young's modulus, particle size and the density of the particle as seen in Eqs. 6-12. Finally on the Fig. 19, the collection efficiency is illustrated with respect to the adhesion parameter. It is clearly seen that a higher adhesion parameter does not correlate directly with a higher collection efficiency but in fact the opposite seems to be true. This is because the adhesion parameter is the measure between adhesive force and the particle inertia [59]. In other words, the parameter acts as a relative measure of the impact process between the particle and the fin. The fouling process of a FTHE is not only a function of the adhesion parameter but also a function of the Stokes number, Reynolds number and the elasticity parameter as shown in this study.

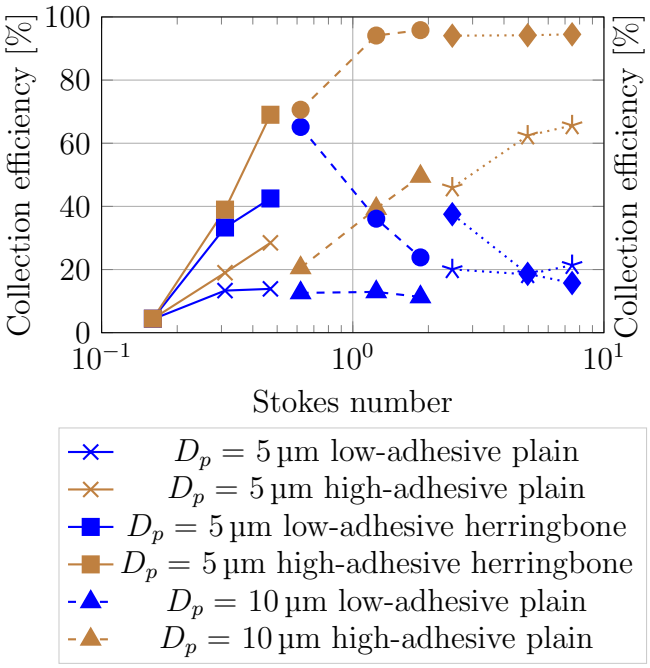

Figure 18: Collection efficiency of all the simulated cases with respect to the Stokes number.

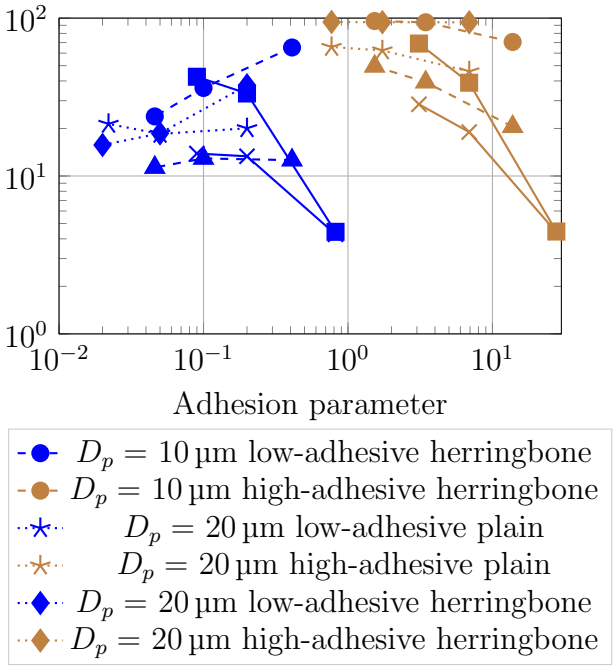

Figure 19: Collection efficiency of all the simulated cases with respect to the Adhesion parameter.

5.4. Fouling rate prediction from air quality measurements

In the earlier sections, the presented numerical results indicated that the fouling process of a FTHE depends monotonically on the Reynolds and Stokes numbers for high-adhesive particles. In contrast, for the low adhesive particles, a non-monotonic relationship was observed. As expected, it was noted that the adhesion and elasticity parameters are equally important in the fouling process. Next, the results will be applied to estimate the fouling rate in a certain FTHE application. The air quality and the particle size distribution of the ambient environment can vary drastically between different applications. For example, the outdoor air during a sandstorm most likely has a much higher concentration of low adhesive particles compared to the indoor air of an average school with high adhesive clothing fibers and other organic substances that are circulated through the heat exchanger. Therefore, when a fouling rate comparison between different fin shapes is performed, it is important to define the particle size distribution and the adhesion properties of the particles in the air.

Next, the present numerical results are applied in the context of the data provided by Cheng and Lin [76]. The data includes the average particle mass size distribution of the air at the Taipei main station during January–February 2008. The measured average particle mass concentrations were $m_c^{4-5\mu m} = 4.37\,\mu g/m^3$, $m_c^{7.5-10\mu m} = 7.42\,\mu g/m^3$ and $m_c^{15-20\mu m} = 10.55\,\mu g/m^3$. The number concentration can then be calculated as $N = m_c/m_p$ where m_p is the weight of one particle. We assume here the diameter of the particle to be the maximum from the size range and its corresponding weight. (D_p = 5, 10, 20 µm) The respective concentrations can then be easily calculated to be $N^{4-5\mu m} = 26\,707\,1/m^3$, $N^{7.5-10\mu m} = 5668\,1/m^3$ and $N^{15-20\mu m} = 1007\,1/m^3$. By knowing the particle concentration N^{d_p} and the corresponding collection efficiency C^{d_p} and the inlet velocity U_{inlet} in Figs. 15-17, it is straightforward to calculate the number fouling rate $F_{number} = N^{d_p} C^{d_p} U_{inlet}$ and the results are shown in Fig. 20.

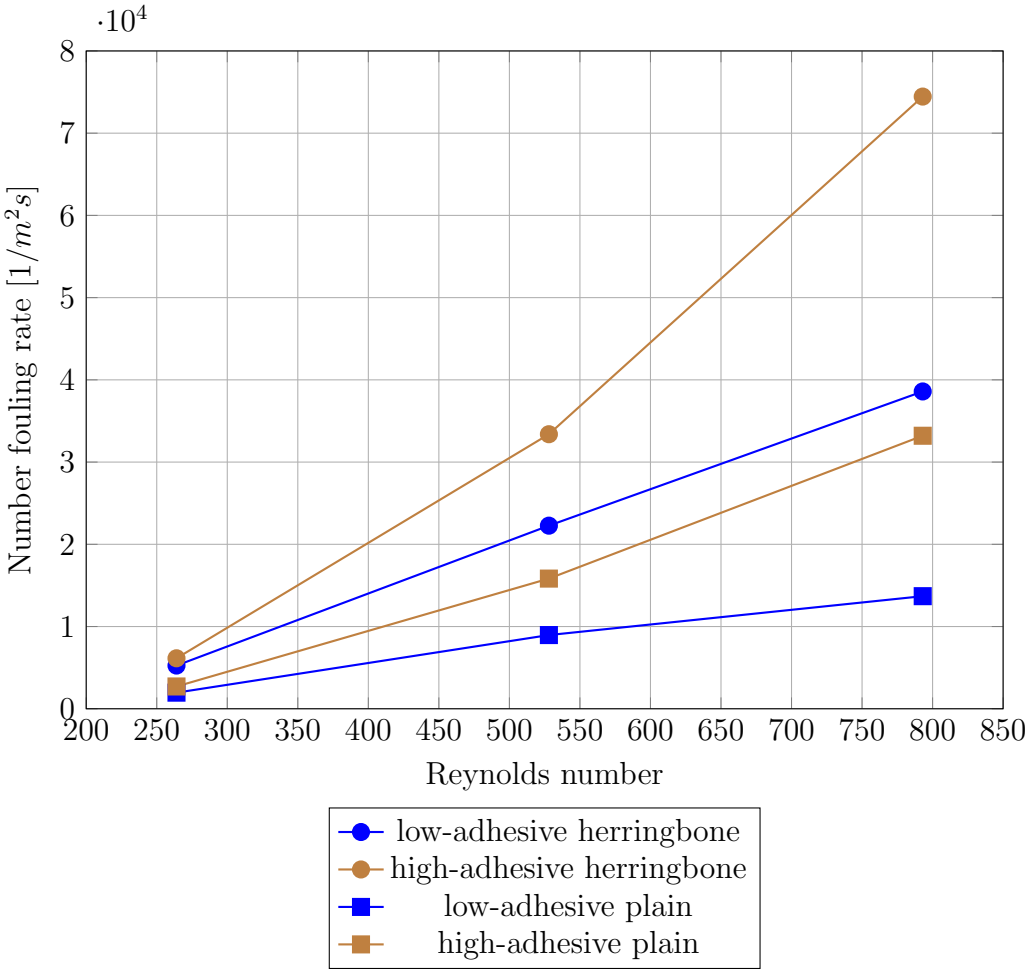

Figure 20: Estimate on the number of overall deposited particles for FTHEs at the Taipei train station.

The thickness of the fouling layer decreases the efficiency of the FTHE in two different ways. First, the fouling layer acts as an insulation in the heat transfer process between the air and the fluid in the tubes. Second, the thickness of the fouling layer will decrease the minimum cross sectional area of the flow and therefore increase the pressure drop over the FTHE. By knowing the volume of each particle size (V_{d_p}), the volume fouling rate can be calculated as $F_{volume} = V_{d_p} F_{number}$. The volume of the deposited particles in unit time for a frontal area of the FTHE can be seen in Fig. 21.

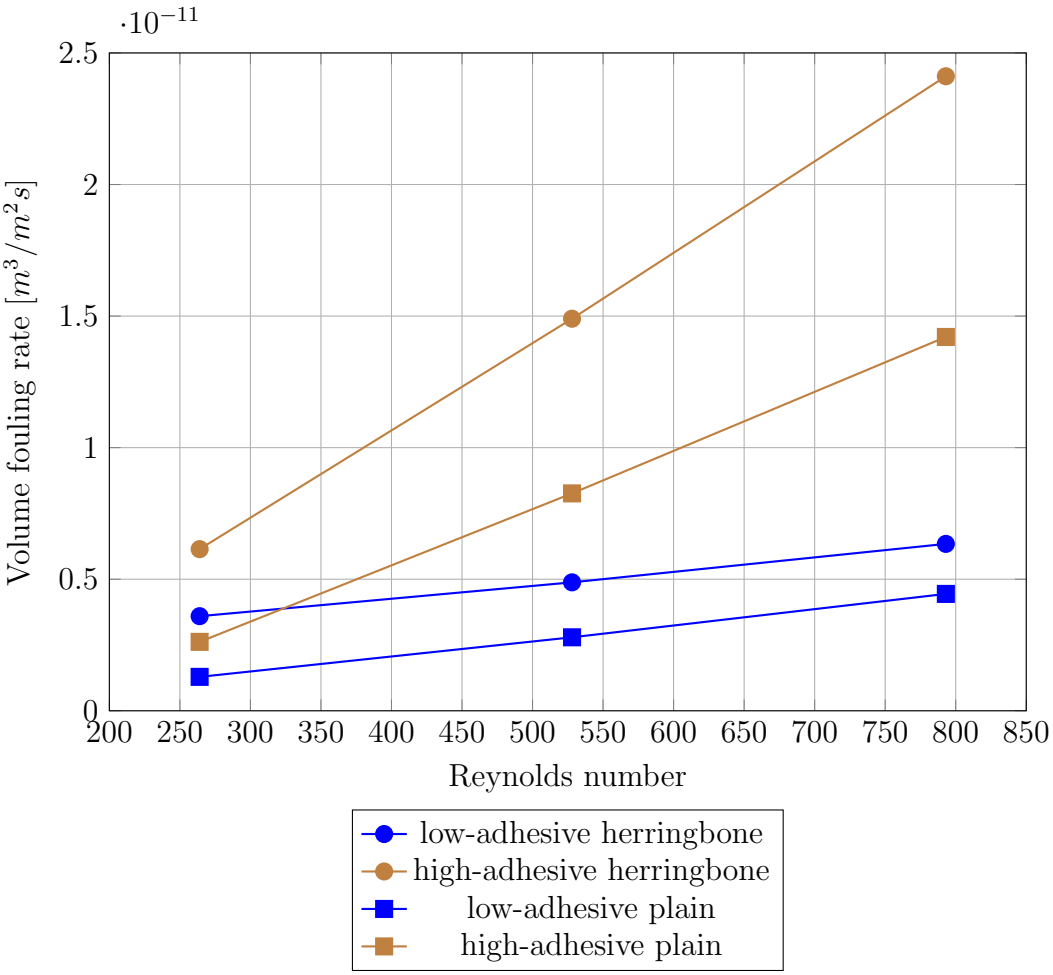

Figure 21: Estimate on the volume of overall deposited particles for FTHEs at the Taipei train station.

First, it is noted that low adhesive particles have a lower volume fouling rate than the high adhesive particles. Second, for a given adhesive type, the plain fin has a lower volume fouling rate than the herringbone fin. It is clear that the volume fouling rate increases with the Reynolds number. If the Reynolds increases by factor 3, the fouling rate is not desired to increase more than by factor 3. The volume fouling rate for low adhesive particles is noted to be 3.45 times higher for Re_{D_h} =793 than at Re_{D_h} =264 in the case of the plain fin shape. In contrast, the herringbone fin shape at Re_{D_h} =793, has a 1.76 times higher volume fouling rate than at Re_{D_h} =264. When the values for the high adhesive particles are compared, the plain fin has a 5.4 times higher volume fouling rate with the highest velocity compared to the lowest. The herringbone has 3.92 times higher volume fouling rate with the highest

velocity compared to the lowest. The main conclusion of the analysis is that the volume fouling rate increases more than by factor 3 in all cases except the herringbone fins with low adhesive particles. As another conclusion, we note that, in the effort to avoid fouling, lower inlet velocities should be used. Indeed, the present results indicate the trade-off between FTHE Reynolds number and the fouling rate. Furthermore, fouling also deteriorates the heat transfer coefficient of a FTHE. Optimally, various parameters including fin type, Reynolds number, air quality, size distribution and particle type should all be known in the design phase.

Last, we note that in practice FTHEs may need to operate in different ambient conditions. Therefore, based on the numerical findings, the type of particles can affect the choice of the optimal fin type. In fact, such design guidelines are already followed in the industry by practical experiences without detailed knowledge on the phenomena. By summing over the fin types and the Reynolds numbers, the fouling volume rate was found to be approximately 3 times higher for the high adhesive particles than for the low adhesive ones.

As discussed earlier, enhanced fin shapes such as herringbone are used to increase the heat transfer on the air side. In an environment with low adhesive particles the volume fouling rate in the nucleation regime is 1.74 times higher for the herringbone fin shape when compared to the plain fin. For the high adhesive particles, the volume fouling rate is 1.8 times higher with herringbone. Together, when both adhesion levels are summed together, the volume fouling rate for the herringbone fin shape is 1.78 times higher when compared to the plain fin FTHE. The presented numerical results indicate the relevance of combined CFD-DEM studies regarding the fouling rate and the performance of the fin during the lifetime of the FTHE.

6. Conclusions

In this study, the deposition of dry particles on a fin-and-tube heat exchanger by a coupled soft-sphere DEM and CFD was performed. The novel selection of material properties for the fouling particles is done such that a representative range of Reynolds numbers, Stokes numbers, elasticity and adhesion parameters is covered. The material selection in this study will lead to critical velocities between the particles and the fin surface that corresponds to the measurements performed for various material combinations and therefore different fouling characteristics. All the different models used for the calculation of the flow field and particle drag were validated. A comparison was carried out between low adhesive and high adhesive particle environments, with particle sizes of D_p = 5, 10, 20µm, with three typical FTHE Reynolds numbers Re_{D_h} =243, 528, 793 and two different fin shapes found in the contemporary HVAC industry. The major findings of this study are summarized below.

1. Novel method for the selection of adhesion properties such as particle size, particle density, effective Young's modulus, Poisson's ratio and adhesion work is demonstrated so that the corresponding critical velocity of the particles represent both ends of the spectrum in the real world fouling environments. The CFD code was validated by comparing the C_d and Strouhal numbers for a free cylinder against literature values. The CFD-DEM code was validated by comparing the particle drag to the analytical values and the DEM code was validated by comparing the critical velocity of the adhesion process to the experimental values reported in the literature.
2. This method enables the comparison of the volume fouling rate of the fin-and-tube heat exchanger fin shapes in different environments.
3. With low adhesive particles, plain fin volume fouling rate is 3.45 times higher with Re_{D_h} =793 than at Re_{D_h} =264. The herringbone fin shape has a volume fouling rate of 1.76 times higher with Re_{D_h} =793 than at Re_{D_h} =264.
4. With high adhesive particles, plain fin volume fouling rate is 5.4 times higher with Re_{D_h} =793 than at Re_{D_h} =264. The herringbone fin shape has a volume fouling rate of 3.92 times higher with Re_{D_h} =793 than at Re_{D_h} =264.

5. High adhesive particles will have 3.0 times higher volume fouling rate than low adhesive particles for both fin shapes, particle sizes and all Reynolds numbers combined.
6. Herringbone fins have 1.74 higher volume fouling rate than plain fin shape for low adhesive type particles. For high adhesive particles, herringbone has 1.8 times higher volume fouling rate and when both particle types are summed together, herringbone has 1.78 times higher volume fouling rate than the plain fin shape.

In the future, the investigated CFD-DEM method could be used for further studies on different fin shapes under different operating conditions and particle properties. Such results would be of high value in design of FTHE's. Novel topics for future research on fouling are different flow control strategies and fin shape optimization. Consequently, it is of constant interest to better manage the costs of FTHE life cycle.

Appendix 1. Deposition locations

Table 3: Collision material properties for Teflon particle and a soda glass wall

Material	E **(GPa)**	ν	ρ **(kg m^{-3})**	w **(J m^{-2})**	**e**
Teflon particle 6 mm	0.4	0.46	2150	0.35	0.8
Soda glass wall	60	0.24	2526	0.13	0.97

Table 4: Collision material properties

Material	E_{eff} **(GPa)**	ν	ρ **(kg m^{-3})**	w **(J m^{-2})**	**e**	V_{crit} **(ms^{-1})**
high-adhesive 5 µm	1.08	0.3	2500	1.04	0.5	5.3
high-adhesive 10 µm	1.08	0.3	2500	1.04	0.5	2.9
high-adhesive 20 µm	1.08	0.3	2500	1.04	0.5	2
low-adhesive 5 µm	1.08	0.3	2500	0.031	0.5	0.34
low-adhesive 10 µm	1.08	0.3	2500	0.031	0.5	0.2
low-adhesive 20 µm	1.08	0.3	2500	0.031	0.5	0.1

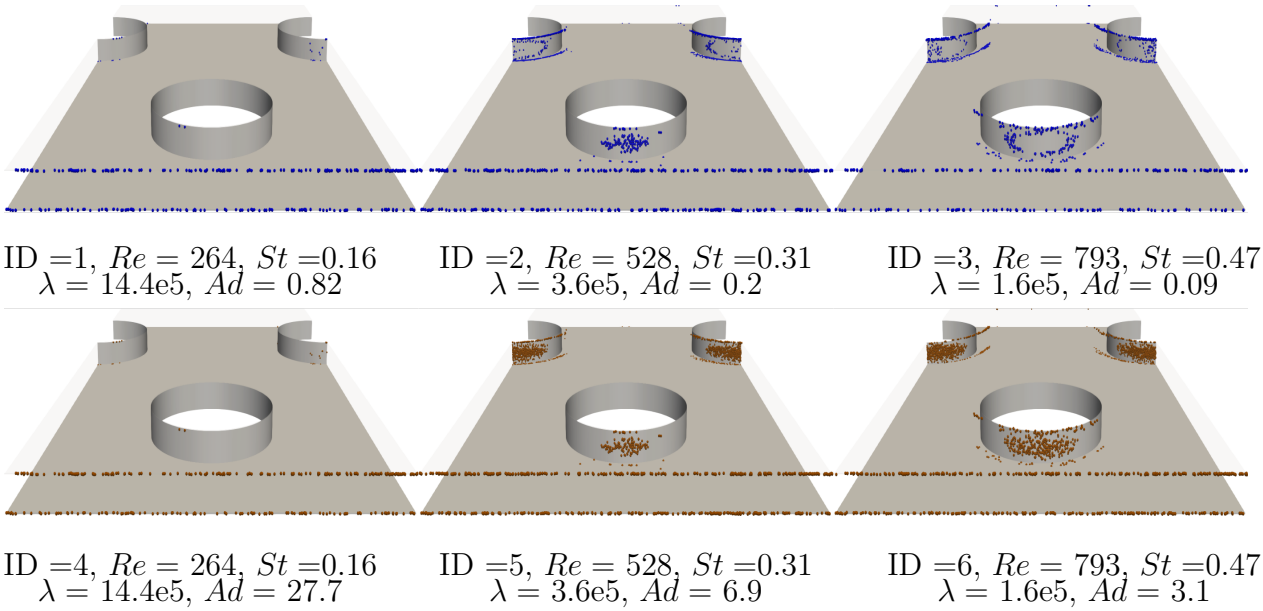

Figure A.1: Deposition locations for plain fin with $D_p = 5\,\mu\text{m}$ • low-adhesive and • high-adhesive particles (size of particles increased by a factor of 60)

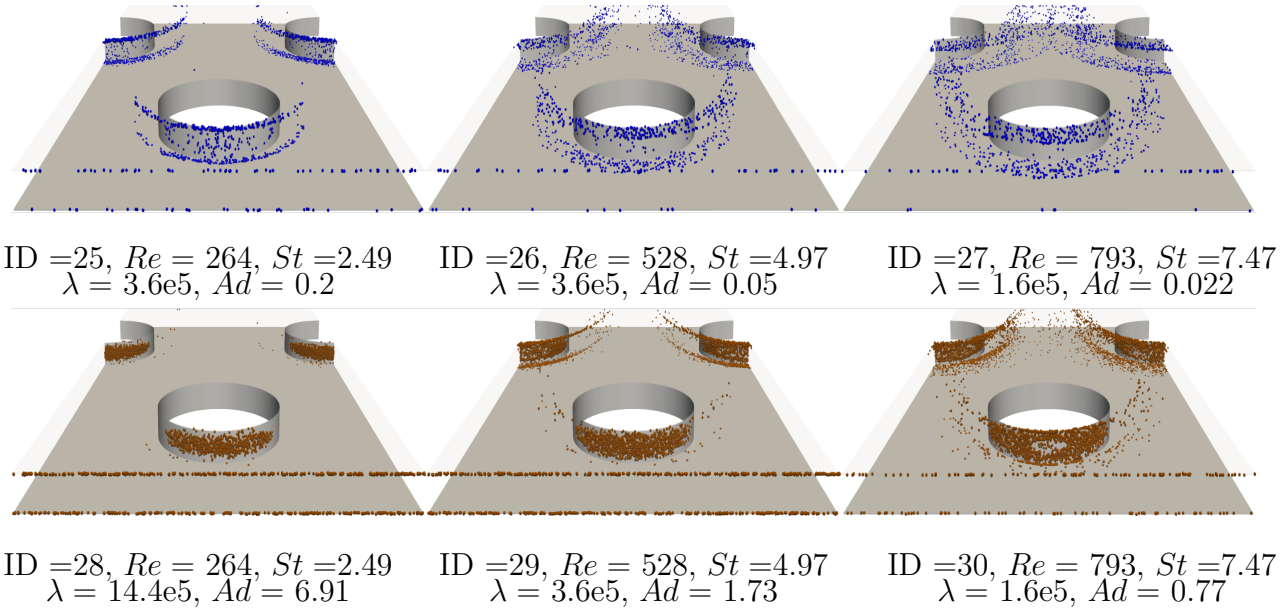

Figure A.2: Deposition locations for plain fin with $D_p = 20\,\mu\text{m}$ • low-adhesive and • high-adhesive particles (size of particles increased by a factor of 15)

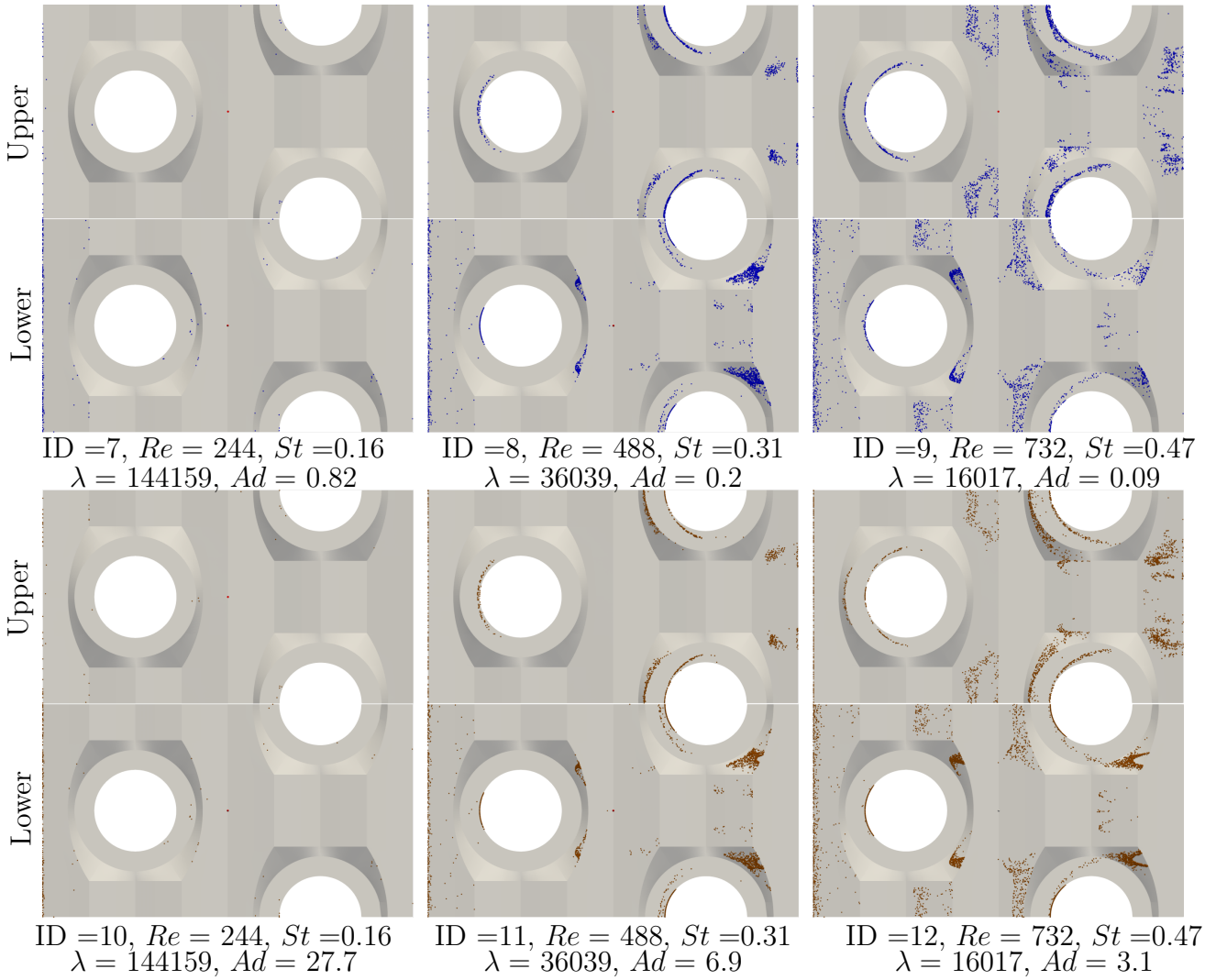

Figure A.3: Deposition locations for lower and upper fin separately with $D_p = 5\,\mu m$ • low-adhesive and • high-adhesive particles (size of particles increased by a factor of 60)

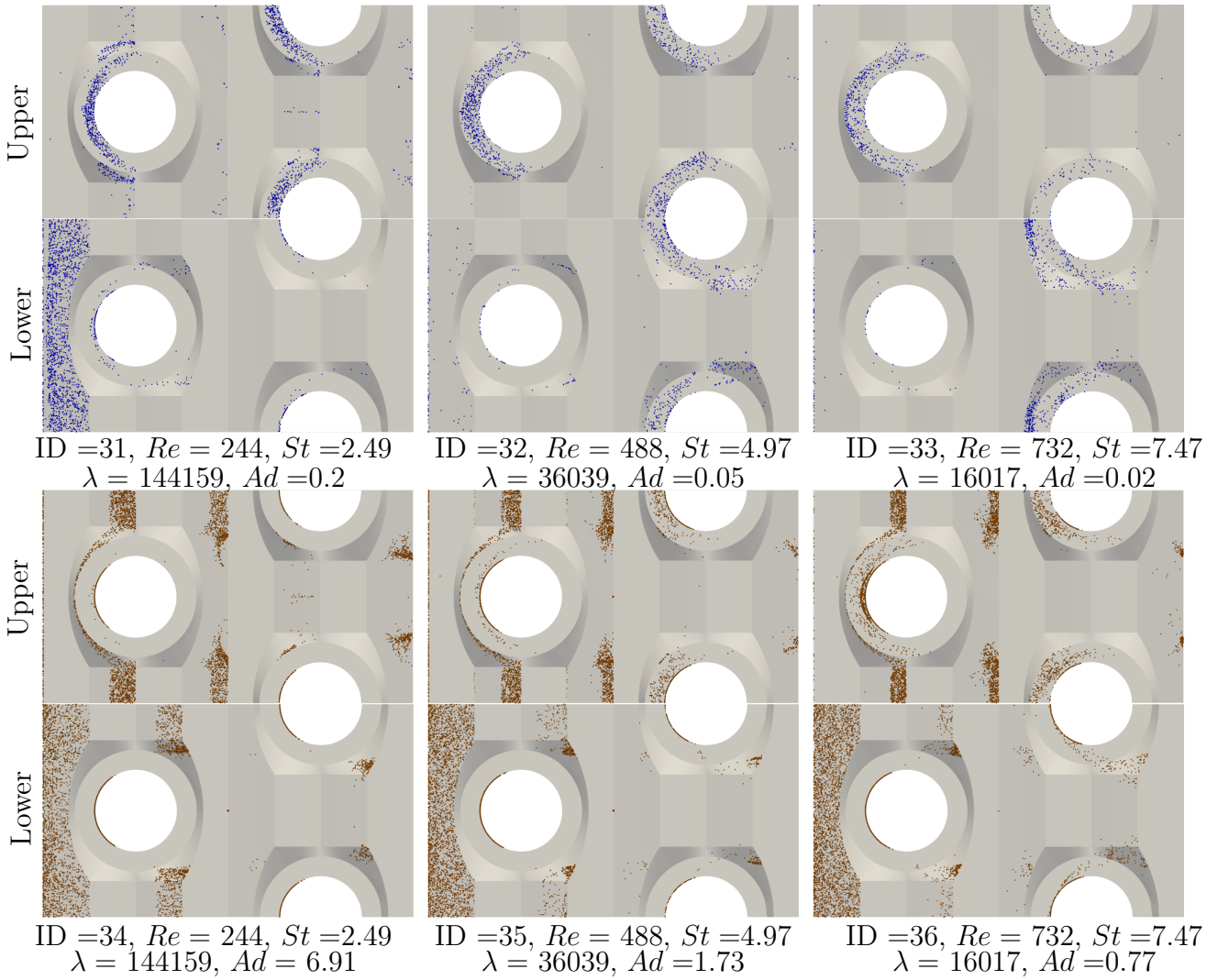

Figure A.4: Deposition locations for lower and upper fin separately with $D_p = 20\,\mu\text{m}$ • low-adhesive and • high-adhesive particles (size of particles increased by a factor of 15)

Acknowledgments

The authors wish to acknowledge CSC – IT Center for Science, Finland, for computational resources and Koja Oy, for financial support.

Nomenclature

Symbols

$\mathbf{u}$	Fluid velocity, ms^{-1}
A_{inlet}	Area of the inlet boundary
A_{min}	Area of the minimum cross section inside the heat exchanger
R_{pf}	local fluid volume fraction, m
u	Velocity, ms^{-1}
U_{inlet}	Inlet flow velocity
$U_{max,avg}$	Maximum average flow velocity
V	Volume of the cell, ms^3
v	Particle velocity, ms^{-1}
x	Cartesian location, m
a	Contact area, m^2
C	Collection efficiency
D_{h}	Hydraulic diameter, mm
E	Young's modulus, Pa
F_{number}	Number fouling rate
F_{volume}	Volume fouling rate
$F_{\mathrm{i,fluid}}$	Particle force, N
n	Surface normal vector
R	Effective particle radius, m
S_n	Material properties parameter for normal direction
S_t	Material properties parameter for tangential direction
w	Adhesion work

Greek symbols

α_f	Local fluid volume fraction, -
μ	Dynamic viscosity of air, $kgm^{-1}s^{-1}$
μ_{sgs}	Eddy viscosity, $kgm^{-1}s^{-1}$
ρ_f	Density of fluid, kgm^{-3}
β	Coefficient restitution parameter
γ	Surface energy density
ν	Poisson's ratio

References

[1] L. Pérez-Lombard, J. Ortiz, C. Pout, A review on buildings energy consumption information, Energy and Buildings 40 (3) (2008) 394 – 398, ISSN 0378-7788, doi: https://doi.org/10.1016/j.enbuild.2007.03.007.

[2] A. F. Mills, A. Mills, Basic heat and mass transfer, vol. 2, Prentice hall Upper Saddle River, 1999.

[3] J. Jeong, C. N. Kim, B. Youn, A study on the thermal contact conductance in fin–tube heat exchangers with 7mm tube, International Journal of Heat and Mass Transfer 49 (7) (2006) 1547 – 1555, ISSN 0017-9310, doi:https://doi.org/10.1016/j.ijheatmasstransfer.2005.10.042.

[4] C.-C. Wang, R. L. Webb, K.-Y. Chi, Data reduction for air-side performance of fin-and-tube heat exchangers, Experimental Thermal and Fluid Science 21 (4) (2000) 218 – 226, ISSN 0894-1777, doi: https://doi.org/10.1016/S0894-1777(00)00005-4.

[5] C.-C. Wang, K.-Y. Chi, C.-J. Chang, Heat transfer and friction characteristics of plain fin-and-tube heat exchangers, part II: Correlation, International Journal of Heat and Mass Transfer 43 (15) (2000) 2693 – 2700, ISSN 0017-9310, doi:https://doi.org/10.1016/S0017-9310(99)00333-6.

[6] T. Välikangas, R. Karvinen, Selected Papers from the 9th International Conference on Computational Heat and Mass Transfer, Heat Transfer Engineering .

[7] Y.-T. Lin, Y.-M. Hwang, C.-C. Wang, Performance of the herringbone wavy fin under dehumidifying conditions, International Journal of Heat and Mass Transfer 45 (25) (2002) 5035 – 5044, ISSN 0017-9310, doi:https://doi.org/10.1016/S0017-9310(02)00193-X.

[8] S. Wongwises, Y. Chokeman, Effect of fin pitch and number of tube rows on the air side performance of herringbone wavy fin and tube heat exchangers, Energy Conversion and Management 46 (13-14) (2005) 2216–2231, ISSN 01968904, doi:10.1016/j.enconman.2004.09.011.

[9] Y. Chokeman, S. Wongwises, Effect of fin pattern on the air-side performance of herringbone wavy

fin-and-tube heat exchangers, Heat and Mass Transfer/Waerme- und Stoffuebertragung 41 (7) (2005) 642–650, ISSN 09477411, doi:10.1007/s00231-004-0578-5.

[10] X. Zhang, D. Tafti, Flow efficiency in multi-louvered fins, International Journal of Heat and Mass Transfer 46 (10) (2003) 1737 – 1750, ISSN 0017-9310, doi:https://doi.org/10.1016/S0017-9310(02)00482-9.

[11] J. Yun, K. Lee, Investigation of heat transfer characteristics on various kinds of fin-and-tube heat exchangers with interrupted surfaces, International Journal of Heat and Mass Transfer 42 (13) (1999) 2375 – 2385, ISSN 0017-9310, doi:https://doi.org/10.1016/S0017-9310(98)00310-X.

[12] T. Välikangas, S. Singh, K. Sørensen, T. Condra, Fin-and-tube heat exchanger enhancement with a combined herringbone and vortex generator design, International Journal of Heat and Mass Transfer 118 (2018) 602 – 616, ISSN 0017-9310, doi:https://doi.org/10.1016/j.ijheatmasstransfer.2017.11.006.

[13] M. Li, H. Zhang, J. Zhang, Y. Mu, E. Tian, D. Dan, X. Zhang, W. Tao, Experimental and numerical study and comparison of performance for wavy fin and a plain fin with radiantly arranged winglets around each tube in fin-and-tube heat exchangers, Applied Thermal Engineering 133 (2018) 298 – 307, ISSN 1359-4311, doi:https://doi.org/10.1016/j.applthermaleng.2018.01.012.

[14] Y. He, H. Han, W. Tao, Y. Zhang, Numerical study of heat-transfer enhancement by punched winglet-type vortex generator arrays in fin-and-tube heat exchangers, International Journal of Heat and Mass Transfer 55 (21) (2012) 5449 – 5458, ISSN 0017-9310, doi: https://doi.org/10.1016/j.ijheatmasstransfer.2012.04.059.

[15] Z. Guan, S. Yu, K. Hooman, H. Gurgenci, J. Barry, Dust characterisation for solar collector deposition and cleaning in a concentrating solar thermal power plant, Heat Exchanger Fouling and Cleaning (2015) 301–307.

[16] B. E. Lee, C. A. Fletcher, S. H. Shin, S. B. Kwon, Computational study of fouling deposit due to surface-coated particles in coal-fired power utility boilers, Fuel 81 (15) (2002) 2001 – 2008, ISSN 0016-2361, doi:https://doi.org/10.1016/S0016-2361(02)00127-8.

[17] M. Waring, J. A. Siegel, Particle loading rates for HVAC filters, heat exchangers, and ducts, Indoor Air 18 (3) (2008) 209–224.

[18] F. Zhan, D. Zhuang, G. Ding, P. Ju, J. Tang, Influence of wet-particle deposition on air-side heat transfer and pressure drop of fin-and-tube heat exchangers, International Journal of Heat and Mass Transfer 124 (2018) 1230 – 1244, ISSN 0017-9310, doi:https://doi.org/10.1016/j.ijheatmasstransfer.2018.04.049.

[19] Y.-C. Ahn, J.-M. Cho, H.-S. Shin, Y.-J. Hwang, C.-G. Lee, J.-K. Lee, H.-U. Lee, T.-W. Kang, An experimental study of the air-side particulate fouling in fin-and-tube heat exchangers of air conditioners, Korean Journal of Chemical Engineering 20 (5) (2003) 873–877.

[20] F.-L. Wang, Y.-L. He, Z.-X. Tong, S.-Z. Tang, Real-time fouling characteristics of a typical heat exchanger used in the waste heat recovery systems, International Journal of Heat and Mass Transfer

104 (2017) 774 – 786, ISSN 0017-9310, doi:https://doi.org/10.1016/j.ijheatmasstransfer.2016.08.112.

[21] X. Li, H. Zhou, K. Cen, Influences of various vortex structures on the dispersion and deposition of small ash particles, Fuel 87 (7) (2008) 1379 – 1382, ISSN 0016-2361, doi: https://doi.org/10.1016/j.fuel.2007.07.007.

[22] L. Mu, L. Zhao, H. Yin, Modelling and measurements of the characteristics of ash deposition and distribution in a HRSG of wastewater incineration plant, Applied Thermal Engineering 44 (2012) 57 – 68, ISSN 1359-4311, doi:https://doi.org/10.1016/j.applthermaleng.2012.03.039.

[23] A. Leppänen, H. Tran, R. Taipale, E. Välimäki, A. Oksanen, Numerical modeling of fine particle and deposit formation in a recovery boiler, Fuel 129 (2014) 45 – 53, ISSN 0016-2361, doi: https://doi.org/10.1016/j.fuel.2014.03.046.

[24] J. A. Siegel, W. W. Nazaroff, Predicting particle deposition on HVAC heat exchangers, Atmospheric Environment 37 (39) (2003) 5587 – 5596, ISSN 1352-2310, doi: https://doi.org/10.1016/j.atmosenv.2003.09.033, indoor Air Chemistry and Physics: Papers from Indoor Air 2002.

[25] H. V. Inamdar, E. A. Groll, J. A. Weibel, S. V. Garimella, Prediction of air-side particulate fouling of HVAC&R heat exchangers, Applied Thermal Engineering 104 (2016) 720 – 733, ISSN 1359-4311, doi:https://doi.org/10.1016/j.applthermaleng.2016.05.082.

[26] B. C. Pak, E. A. Groll, J. E. Braun, Impact of Fouling and Cleaning on Plate Fin and Spine Fin Heat Exchanger Performance., ASHRAE Transactions 111 (1).

[27] D. Bouris, G. Bergeles, Numerical calculation of the effect of deposit formation on heat-exchanger efficiency, International Journal of Heat and Mass Transfer 40 (17) (1997) 4073 – 4084, ISSN 0017-9310, doi:https://doi.org/10.1016/S0017-9310(97)00058-6.

[28] H. Han, Y.-L. He, W.-Q. Tao, Y.-S. Li, A parameter study of tube bundle heat exchangers for fouling rate reduction, International Journal of Heat and Mass Transfer 72 (2014) 210 – 221, ISSN 0017-9310, doi:https://doi.org/10.1016/j.ijheatmasstransfer.2014.01.010.

[29] F.-L. Wang, Y.-L. He, S.-Z. Tang, Z.-X. Tong, Parameter study on the fouling characteristics of the H-type finned tube heat exchangers, International Journal of Heat and Mass Transfer 112 (Supplement C) (2017) 367 – 378, ISSN 0017-9310, doi:https://doi.org/10.1016/j.ijheatmasstransfer.2017.04.107.

[30] Y. Wang, G. Tang, Numerical investigation on the coupling of ash deposition and acid vapor condensation on the H-type fin tube bank, Applied Thermal Engineering 139 (2018) 524 – 534, ISSN 1359-4311, doi:https://doi.org/10.1016/j.applthermaleng.2018.05.026.

[31] C. Zhang, Z. Tang, Z. Zhang, J. Shi, J. Chen, M. Zhang, Impact of airside fouling on microchannel heat exchangers, Applied Thermal Engineering 128 (Supplement C) (2018) 42 – 50, ISSN 1359-4311, doi:https://doi.org/10.1016/j.applthermaleng.2017.08.163.

[32] I. H. Bell, E. A. Groll, H. König, Experimental analysis of the effects of particulate fouling on heat exchanger heat transfer and air-side pressure drop for a hybrid dry cooler, Heat Transfer Engineering 32 (3-4) (2011) 264–271.

[33] I. H. Bell, E. A. Groll, Air-side particulate fouling of microchannel heat exchangers: Experimental comparison of air-side pressure drop and heat transfer with plate-fin heat exchanger, Applied Thermal Engineering 31 (5) (2011) 742 – 749, ISSN 1359-4311, doi: https://doi.org/10.1016/j.applthermaleng.2010.10.019, mNF 2009 Special Issue.

[34] F. Zhan, J. Tang, G. Ding, D. Zhuang, Experimental investigation on particle deposition characteristics of wavy fin-and-tube heat exchangers, Applied Thermal Engineering 99 (2016) 1039 – 1047, ISSN 1359-4311, doi:https://doi.org/10.1016/j.applthermaleng.2016.01.136.

[35] F. Zhan, D. Zhuang, G. Ding, J. Tang, Numerical model of particle deposition on fin surface of heat exchanger, International Journal of Refrigeration 72 (2016) 27 – 40, ISSN 0140-7007, doi: https://doi.org/10.1016/j.ijrefrig.2016.07.015.

[36] E. Sauret, K. Hooman, Particle size distribution effects on preferential deposition areas in metal foam wrapped tube bundle, International Journal of Heat and Mass Transfer 79 (2014) 905 – 915, ISSN 0017-9310, doi:https://doi.org/10.1016/j.ijheatmasstransfer.2014.08.038.

[37] S. T. Kuruneru, E. Sauret, S. C. Saha, Y. T. Gu, A coupled finite volume & discrete element method to examine particulate foulant transport in metal foam heat exchangers, International Journal of Heat and Mass Transfer 115 (2017) 43–61.

[38] S. T. Kuruneru, E. Sauret, S. C. Saha, Y. Gu, Coupled CFD-DEM simulation of oscillatory particle-laden fluid flow through a porous metal foam heat exchanger: Mitigation of particulate fouling, Chemical Engineering Science 179 (2018) 32 – 52, ISSN 0009-2509, doi: https://doi.org/10.1016/j.ces.2018.01.006.

[39] S. T. Kuruneru, E. Sauret, S. C. Saha, Y. T. Gu, A coupled finite volume & discrete element method to examine particulate foulant transport in metal foam heat exchangers, International Journal of Heat and Mass Transfer 115 (2017) 43 – 61, ISSN 0017-9310, doi: https://doi.org/10.1016/j.ijheatmasstransfer.2017.07.027.

[40] S. T. Kuruneru, E. Sauret, K. Vafai, S. C. Saha, Y. Gu, Analysis of particle-laden fluid flows, tortuosity and particle-fluid behaviour in metal foam heat exchangers, Chemical Engineering Science 172 (2017) 677 – 687, ISSN 0009-2509, doi:https://doi.org/10.1016/j.ces.2017.07.027.

[41] W. Pirompugd, C.-C. Wang, S. Wongwises, Correlations for wet surface ratio of fin-and-tube heat exchangers, International Journal of Heat and Mass Transfer 53 (1) (2010) 568 – 573, ISSN 0017-9310, doi:https://doi.org/10.1016/j.ijheatmasstransfer.2009.09.025.

[42] S. Elgobashi, An updated classification map of particle-laden turbulent flows, in: IUTAM Symposium

on Computational Approaches to Multiphase Flow, Springer, 3–10, 2006.

[43] R. I. Issa, Solution of the implicitly discretised fluid flow equations by operator-splitting, Journal of computational physics 62 (1) (1986) 40–65.

[44] C. Goniva, C. Kloss, N. G. Deen, J. A. Kuipers, S. Pirker, Influence of rolling friction on single spout fluidized bed simulation, Particuology 10 (5) (2012) 582–591.

[45] T. O. Foundation, The OpenFOAM Documentation, URL `https://openfoam.org/`, 2017.

[46] C. Kloss, C. Goniva, A. Hager, S. Amberger, S. Pirker, Models, algorithms and validation for opensource DEM and CFD–DEM, Progress in Computational Fluid Dynamics, an International Journal 12 (2-3) (2012) 140–152.

[47] F. Nicoud, F. Ducros, Subgrid-scale stress modelling based on the square of the velocity gradient tensor, Flow, turbulence and Combustion 62 (3) (1999) 183–200.

[48] M. Mirzaei, A. Sohankar, L. Davidson, F. Innings, Large Eddy Simulation of the flow and heat transfer in a half-corrugated channel with various wave amplitudes, International Journal of Heat and Mass Transfer 76 (2014) 432 – 446, ISSN 0017-9310, doi: https://doi.org/10.1016/j.ijheatmasstransfer.2014.04.018.

[49] R. Nagaosa, Turbulence model-free approach for predictions of air flow dynamics and heat transfer in a fin-and-tube exchanger, Energy Conversion and Management 142 (2017) 414–425, doi: 10.1016/j.enconman.2017.03.063, cited By 0.

[50] P. A. Cundall, O. D. Strack, A discrete numerical model for granular assemblies, geotechnique 29 (1) (1979) 47–65.

[51] S. Benyahia, M. Syamlal, T. J. O'Brien, Extension of Hill–Koch–Ladd drag correlation over all ranges of Reynolds number and solids volume fraction, Powder Technology 162 (2) (2006) 166 – 174, ISSN 0032-5910, doi:https://doi.org/10.1016/j.powtec.2005.12.014.

[52] R. J. Hill, D. L. Koch, A. J. Ladd, The first effects of fluid inertia on flows in ordered and random arrays of spheres, Journal of Fluid Mechanics 448 (2001) 213–241.

[53] D. L. Koch, R. J. Hill, Inertial effects in suspension and porous-media flows, Annual Review of Fluid Mechanics 33 (1) (2001) 619–647.

[54] H. Hamaker, The London—van der Waals attraction between spherical particles, physica 4 (10) (1937) 1058–1072.

[55] K. L. Johnson, K. Kendall, A. Roberts, Surface energy and the contact of elastic solids, Proc. R. Soc. Lond. A 324 (1558) (1971) 301–313.

[56] D. Tabor, Surface forces and surface interactions, in: Plenary and Invited Lectures, Elsevier, 3–14, 1977.

[57] J. N. Israelachvili, Intermolecular and surface forces, Academic press, 2011.

[58] E. J. Parteli, J. Schmidt, C. Blümel, K.-E. Wirth, W. Peukert, T. Pöschel, Attractive particle interaction forces and packing density of fine glass powders, Scientific reports 4 (2014) 6227.

[59] J. S. Marshall, S. Li, Adhesive particle flow, Cambridge University Press, 2014.

[60] V. Armenio, U. Piomelli, V. Fiorotto, Effect of the subgrid scales on particle motion, Physics of Fluids 11 (10) (1999) 3030–3042.

[61] J. Hærvig, K. Sørensen, T. Condra, Early stages of agglomeration of adhesive particles in fully-developed turbulent pipe flows, International Journal of Multiphase Flow 106 (2018) 254 – 267, ISSN 0301-9322, doi:https://doi.org/10.1016/j.ijmultiphaseflow.2018.04.017.

[62] D. Labbé, P. Wilson, A numerical investigation of the effects of the spanwise length on the 3-D wake of a circular cylinder, Journal of Fluids and Structures 23 (8) (2007) 1168 – 1188, ISSN 0889-9746, doi:https://doi.org/10.1016/j.jfluidstructs.2007.05.005.

[63] V. Kalro, T. Tezduyar, Parallel 3D computation of unsteady flows around circular cylinders, Parallel Computing 23 (9) (1997) 1235 – 1248, ISSN 0167-8191, doi:https://doi.org/10.1016/S0167-8191(97)00050-1, parallel computing methods in applied fluid mechanics.

[64] R. D. Henderson, Nonlinear dynamics and pattern formation in turbulent wake transition, Journal of Fluid Mechanics 352 (1997) 65–112.

[65] C. Wieselberger, 'Neurere feststellungen über die gesetze des flussigkeitsund luftwiederstands, 1921.

[66] L. Li, B. Li, Z. Liu, Modeling of spout-fluidized beds and investigation of drag closures using OpenFOAM, Powder Technology 305 (2017) 364 – 376, ISSN 0032-5910, doi:https://doi.org/10.1016/j.powtec.2016.10.005.

[67] H. Kuuluvainen, A. Arffman, A. Järvinen, J. Harra, J. Keskinen, The effect of materials and obliquity of the impact on the critical velocity of rebound, Aerosol Science and Technology 51 (3) (2017) 301–310.

[68] S. Wall, W. John, H.-C. Wang, S. L. Goren, Measurements of kinetic energy loss for particles impacting surfaces, Aerosol Science and Technology 12 (4) (1990) 926–946.

[69] H.-C. Wang, W. John, Dynamic contact charge transfer considering plastic deformation, Journal of aerosol science 19 (4) (1988) 399–411.

[70] L. Rogers, J. Reed, The adhesion of particles undergoing an elastic-plastic impact with a surface, Journal of Physics D: Applied Physics 17 (4) (1984) 677.

[71] T. D'Ottavio, S. L. Goren, Aerosol capture in granular beds in the impaction dominated regime, Aerosol Science and Technology 2 (2) (1982) 91–108.

[72] Y.-S. Cheng, H.-C. Yeh, Particle bounce in cascade impactors., Environmental Science & Technology 13 (11) (1979) 1392–1396.

[73] N. A. Esmen, P. Ziegler, R. Whitfield, The adhesion of particles upon impaction, Journal of Aerosol Science 9 (6) (1978) 547–556.

[74] J. Derksen, H. Van den Akker, S. Sundaresan, Two-way coupled large-eddy simulations of the gas-solid flow in cyclone separators, AIChE Journal 54 (4) (2008) 872–885.

[75] J. D. Schwarzkopf, M. Sommerfeld, C. T. Crowe, Y. Tsuji, Multiphase flows with droplets and particles, CRC press, 2011.

[76] Y.-H. Cheng, Y.-L. Lin, Measurement of particle mass concentrations and size distributions in an underground station, Aerosol Air Qual. Res 10 (2010) 22–29.